Direct Numerical Simulation of a transitional mixing layer laden with multicomponent-fuel evaporating drops using continuous thermodynamics

By PATRICK C. LE CLERCQ and JOSETTE BELLAN

Jet Propulsion Laboratory, MS 125-109, California Institute of Technology, Pasadena, CA 91109-8099, USA

(Received 2 May 2002)

A model of a temporal three-dimensional mixing layer laden with fuel drops of a liquid containing a large number of species is derived. The drop model is based on continuous thermodynamics, whereby the fuel composition is statistically described through a distribution function that depends solely on the chemical species molar weight. The drop temperature is initially lower than that of the carrier gas, leading to drop heat up and evaporation. The model describing the changes in the multicomponent (MC) fuel drop composition and in the gas phase composition due to evaporation, encompasses only two more conservation equations when compared with the equivalent single-component (SC) fuel formulation. A simulation of a single, isolated drop of an MC-fuel having a sharply peaked distribution is shown to compare favorably with an equivalent SC-fuel drop simulation. The new physics embedded in the MC formulation is demonstrated by comparing results from MC-fuel drops with those of an SC-fuel typically used to represent the MC-fuel. Further, two mixing layer simulations are conducted with MC-fuel

they are compared to equivalent SC-fuel simulations conducted elsewhere (Okong'o & Bellan (2002a)). Analysis of the results shows that although the global layer characteristics are generally similar in the SC and MC situations, the MC layers display a higher momentum-thickness base Reynolds number at transition. Vorticity and helicity-density analyses show that the SC layers exhibit larger vortical activity and RMS knottedness than their MC counterpart. An examination of the drop organization shows more structure and an increased drop-number density for MC simulations in regions of moderate and high strain. These results are primarily attributed to the slower evaporation of MC-fuel drops than of their SC counterpart, primarily due to the lower volatility of the higher molar weight species, and also to condensation of these species on drops transported in regions of different gas composition. This evaporation/condensation process is also responsible for the decreased drop-size polydispersity observed in the MC layers. The more volatile species released in the gas phase earlier during the drop lifetime reside in the lower stream while intermediary molar weight species are entrained in the mixing layer; the heavier species that evaporate later during the drop lifetime tend to reside in regions of high drop number density. This leads to a segregation of species in the gas phase based on the relative evaporation time from the drops. Neither this species segregation, nor the decreased drop-size polydispersity, nor the drop temperature variation with respect to the initial temperature or as a function of the mass loading can be captured by the SC-fuel simulations.

---

1. Introduction

Most power producing combustion devices employ sprays of commercial petroleum fuels that typically contain hundreds of pure species. Despite the preponderance of mul-

ticomponent (MC) fuels, the specific behavior of such sprays in turbulent flows is not well understood when compared to that of single-component (SC) fuel sprays. Given the complexities of spatial sprays in combustion chambers, simpler geometric configurations, such as mixing layers, seem to be a reasonable starting point for fundamental studies. Moreover, considering the complexities associated with spatial mixing layer boundary conditions, temporal mixing layers appear as the simplest pertinent configuration. The goal of the present study is to understand the specific difference between MC-fuel and SC-fuel drop-laden mixing layer characteristics.

To achieve this goal, the present study employs Direct Numerical Simulation (DNS) to investigate the behavior of a temporal mixing layer whose lower stream is initially laden with a large number of evaporating MC-fuel drops. DNS studies with solid particles in the absence of phase change were previously performed by Boivin *et al.* (1998), and by Mashayek & Jaberi (1999) in the context of isotropic turbulence; by Mashayek (1998a), who investigated evaporating drops in isotropic turbulence; by Réveillon & Vervisch (2000) who studied clusters and randomly-distributed evaporating SC-fuel drops in a three-dimensional (3D) freely decaying turbulence; by Mashyek (1998b) who explored evaporating drops in homogeneous shear; and by Miller & Bellan (1999) and Miller & Bellan (2000) who studied 3D mixing layers with evaporating SC-fuel drops. The present DNS methodology generally follows that of Miller & Bellan (1999), while the drop model is entirely novel in the context of mixing layers. The change in the drop model induces corresponding changes in the mixing layer model. The introduction of the specific MC-fuel drop model is motivated by the observation that it may be impractical to model mixtures composed of a large number of species by accounting for each individual constituent (e.g. see the single drop, binary-fuel model of Harstad & Bellan (1991) and the MC-fuel drop model of Law & Law (1982)). Therefore, the strategy adopted herein

is to use the statistical point of view embedded in the Continuous Thermodynamics (CT) approach. The CT approach was discussed in detail by Gal-Or *et al.* (1975) who derived a self-consistent theory based on this concept, and by Cotterman *et al.* (1985) in the context of phase equilibrium calculations. Based on the CT approach, Tamim & Hallett (1995) and Hallett (2000) have developed a model for the evaporation of a single, isolated drop of fuel that is a mixture of very many species. Furthermore, the same model has been used by Lippert & Reitz (1997) as a building block in codes devoted to practical applications. The present study adopts the CT approach and utilizes it in a fundamental study of the coupled interaction between a multitude of drops and the flow in a temporal mixing layer at atmospheric pressure.

In § 2 we recall the CT model in the context of a single drop and derive the CT model for a mixing layer. The potential of the CT model is demonstrated in § 3 by first comparing its predictions with SC-fuel models and then assessing its qualitative behavior for MC fuels. Mixing layer results are presented in § 4. These encompass global characteristics, detailed visualizations, calculations of probability density functions (PDFs) and first order statistics. The emerging picture is that of important differences between the predictions of SC- and MC-fuel models.

2. Mathematical model

The governing equations are formulated for the temporal mixing layer in an Eulerian-Largrangian frame for the gas and drops, respectively. This representation is consistent with the volumetrically small loading ($\simeq 10^{-3}$), although the mass loading can be substantial due to the very high density ratio between the liquid and carrier gas ($O(10^3)$). Moreover, the drops are treated as point sources of mass, momentum and energy. This representation is consistent with the drop size being smaller than the Kolmogorov scale

(see discussion in Boivin *et al.* (1998)). Unsteady drag and added mass effects are neglected, as well as Basset history forces, all of which are small for liquid/gas density ratios (Boivin *et al.* (1998)); further neglected are drop collisions. Moreover, the carrier gas is assumed calorically perfect.

2.1. *Continuous thermodynamics for single multicomponent-fuel drops*

The primary idea of CT modeling is to describe the fuel composition (both liquid or vapor) using a distribution function, f. Although generally f depends on many parameters representing the characteristics of the fuels, it has been shown (Cotterman *et al.* (1985), Hallett (2000)) that in certain cases it is possible to reduce this dependency to a single parameter: the species molar weight. This simplification is available for mixtures composed of homologous species (Gal-Or *et al.* (1975), Cotterman *et al.* (1985)) and includes diesel and gasoline fuels (Cotterman *et al.* (1985), Tamim & Hallett (1995)), both of which are of major practical interest. The advantage of such a statistical description is that while a wide range of individual species can be accommodated in the mixture, the number of governing equations is minimally augmented with respect to that necessary for a single species because the composition is represented by a small number of parameters determining f.

In CT, f is used to define the mole fraction of species α, X_α, whose molar weight lies within the range m_α to $m_\alpha + \Delta m_\alpha$ through

$$X_\alpha = f(m_\alpha)\Delta m_\alpha \tag{2.1}$$

with the normalization condition

$$\int_0^\infty f(m_\alpha)\, dm_\alpha = 1. \tag{2.2}$$

Because mixtures always contain a finite number of individual species, in all CT applications f is non-null only in a finite interval (Gal-Or *et al.* (1975)). Whitson (1983) has

shown that gamma distributions may be used to characterize the molar weight of crude oils through

$$f(m_\alpha) = \frac{(m_\alpha - \gamma)^{\zeta-1}}{\beta^\zeta \Gamma(\zeta)} \exp\left[-\left(\frac{m_\alpha - \gamma}{\beta}\right)\right], \tag{2.3}$$

where $\Gamma(\zeta) = \int_0^\infty \xi^{\zeta-1} e^{-\zeta} d\xi$. The origin of f is specified by γ, and its shape is determined by two parameters, ζ and β. These parameters are related to the mean, θ, the variance, σ^2, and the second moment, ψ, of f by $\theta = \zeta\beta + \gamma$, $\sigma^2 = \zeta\beta^2$ and $\psi = \theta^2 + \sigma^2$.

2.1.1. *Gas-phase conservation equations*

If the overall vapor mole fraction is X_v, the carrier gas mole fraction is $X_{ga} = 1 - X_v$, and the vapor phase mole fraction of species α is defined through

$$X_\alpha = X_v[f_v(m_\alpha)]\Delta m_\alpha. \tag{2.4}$$

Multiplying eq. 2.1 by m_α and by m_α^2 and integrating it for infinitesimally small Δm_α, yields the mean molar weight of the vapor, $\theta_v = \int_0^\infty f_v(m_\alpha) m_\alpha dm_\alpha$ and the second moment $\psi_v = \int_0^\infty f_v(m_\alpha) m_\alpha^2 dm_\alpha$, respectively.

In discrete form, the mean molar weight, m, is defined as

$$m = m_{ga} X_{ga} + \sum_{\alpha=1}^{N} m_\alpha X_\alpha \quad \alpha \in \text{fuel}, \tag{2.5}$$

where N is the total number of species in the fuel, and the equivalent expression in continuous form is

$$m = m_{ga}(1 - X_v) + \theta_v X_v. \tag{2.6}$$

The gas phase is considered to be a mixture of perfect gases and thus

$$p = \frac{\rho R_u T}{m} = c R_u T \tag{2.7}$$

where $\rho = mc$ is the mass density of the gas mixture, p is the thermodynamic pressure, R_u is the universal gas constant, T is the temperature and c is the molar density.

The CT gas-phase conservation equations are derived as in Tamim & Hallett (1995)

from the unsteady discrete form of the molar fraction conservation and enthalpy equations

$$\frac{\partial(cX_\alpha)}{\partial t} + \nabla \cdot (cX_\alpha \mathbf{u}^*) = \nabla \cdot (cD_\alpha \nabla X_\alpha), \tag{2.8}$$

$$C_{pv}\frac{\partial(cT)}{\partial t} + C_{pv}\nabla \cdot (cT\mathbf{u}^*) = \nabla \cdot (\lambda_v \nabla T) - \nabla \cdot \left(\sum_{\alpha=1}^{N} \mathbf{J}_{D\alpha} h_{v\alpha}\right). \tag{2.9}$$

This CT derivation involves (1) substituting X_α by $X_v f(m_\alpha)$, integrating eq 2.8 over dm_α and taking the first two moments of eq. 2.8, which leads to conservation equations for $cX_\alpha, cX_\alpha m_\alpha, cX_\alpha m_\alpha^2$, and (2) integrating eq. 2.9 over dm_α to yield a conservation equation for cT. Since a detailed derivation is available in Tamim & Hallett (1995), only a succinct exposition is presented herein. In eqs. 2.8 and 2.9, t is the time, $\mathbf{u}^*$ is the molar average velocity, D_α is the diffusivity of species α in the mixture, C_{pv} is the vapor molar heat capacity at constant pressure, λ is the thermal conductivity, $\mathbf{J}_{D\alpha} = -cD_\alpha \nabla X_\alpha$ is the diffusional molar flux of species α, and $h_{v\alpha}$ is the enthalpy of the α-species in the gas phase. Further, due to the large liquid/gas density ratio, the gas phase can be considered quasi-steady with respect to the liquid phase. Thus, the gas-phase conservation equations are further simplified to yield

$$\nabla \cdot (cX_v \mathbf{u}^*) = \nabla \cdot (c\overline{D}\ \nabla X_v), \tag{2.10}$$

$$\nabla \cdot (cX_v \theta_v \mathbf{u}^*) = \nabla \cdot [c\widetilde{D}\ \nabla(X_v \theta_v)], \tag{2.11}$$

$$\nabla \cdot (cX_v \psi_v \mathbf{u}^*) = \nabla \cdot [c\widehat{D}\ \nabla(X_v \psi_v)], \tag{2.12}$$

$$\overline{C}_{pv}\nabla \cdot (cT\mathbf{u}^*) = \nabla \cdot (\lambda_v\ \nabla T) + [(R_u A_c T - C_{pga}T)c\overline{D} + R_u B_c c\widetilde{D}\ T\ \theta_v]\nabla X_v, \tag{2.13}$$

where additional simplifications have been performed by neglecting the difference of terms that are approximately equal (Tamim & Hallett (1995)). Several averaging definitions were introduced in eqs. 2.10 - 2.13 using the CT form of the diffusivity, $D(m_\alpha)$, and heat

capacity, $C_{pv}(m_\alpha)$

$$\overline{D} = \int_0^\infty D(m_\alpha) f_v(m_\alpha) dm_\alpha, \tag{2.14}$$

$$\widetilde{D}\ \theta_v = \int_0^\infty D(m_\alpha) f_v(m_\alpha) m_\alpha dm_\alpha, \tag{2.15}$$

$$\widehat{D}\ \psi_v = \int_0^\infty D(m_\alpha) f_v(m_\alpha) m_\alpha^2 dm_\alpha, \tag{2.16}$$

$$\overline{C}_{pv} = X_v \int_0^\infty C_{pv}(m_\alpha) f_v(m_\alpha) dm_\alpha + (1 - X_v) C_{pga}, \tag{2.17}$$

having used, as in Tamim & Hallett (1995), the correlation of Chou & Prausnitz (1986)

$$C_{pv}(m_\alpha) = R_u \left[A_c(T_s) + B_c(T_s) m_\alpha \right] \tag{2.18}$$

where the subscript s labels the drop surface. Similar to $C_{pv}(m_\alpha)$, correlations are also available for $D(m_\alpha) = (A_D + B_D m_\alpha)\Phi_D(T)$ with $\Phi_D(T) = T^{5/2}/(B_\Phi + T)$ that can approximately reproduce the diffusional behavior of the α-species in the mixture; the constants A_D, B_D and B_Φ are listed in Tamim & Hallett (1995).

2.1.2. *Liquid-phase conservation equations*

The conservation equations for the liquid phase are here obtained under the assumption of a well-mixed liquid, meaning that internal circulation is very effective and renders the properties of the drop uniform in a time much shorter than the drop lifetime. This assumption is consistent with the slow evaporation limit, which is the situation encountered in the present mixing layer simulations. Departures from this well-mixed state are expected to become increasingly important with wider separation of the saturation vapor-pressure curves for different species, however, for a continuous mixture these departures may be considerably reduced. Following the CT derivation and approximations of Tamim & Hallett (1995), including the assumption of constant liquid mass-density, ρ_l, the conservation equations for a spherically symmetric drop are

$$J_{rs}(1 - X_{vs}) = -c\overline{D}\ (\nabla X_v)_s, \tag{2.19}$$

$$\frac{d\theta_l}{dt} = \frac{6}{c_l d}[J_r(\theta_l - \theta_v X_v) + c\widetilde{D}\ \nabla(X_v\theta_v)]_s, \tag{2.20}$$

$$\frac{d\psi_l}{dt} = \frac{6}{c_l d}[J_r(\psi_l - \psi_v X_v) + c\widehat{D}\ \nabla(X_v\psi_v)]_s, \tag{2.21}$$

$$\frac{dT_d}{dt} = \frac{6}{C_{pl}c_l d}[q_s - L_v], \tag{2.22}$$

where $J_{rs} = (d\mathcal{N}_d/dt)A$ is the radial molar flux at the drop surface, $\mathcal{N}_d = M_d/\theta_l$ is the number of moles in the drop, M_d is the drop mass (subscripts d and l refer to the drop and liquid), $A = \pi d^2/4$ is the drop area, d is the drop diameter, c_l is the liquid molar density ($c_l\rho_l/\theta_l$), C_{pl} is the liquid heat capacity at constant pressure, q_s is the heat flux at the drop surface and L_v is the liquid latent heat. The rapid mixing assumption implies that $T_d = T_s$.

2.1.3. *Boundary conditions*

The boundary conditions are applied both in the far field of the drop and at the drop surface where special care must be devoted to obtain a consistent phase coupling. The far field values of the dependent variables are specified through the given gas composition and temperature; all these values are denoted by the subscript e.

To ensure consistency in the definition of gas and liquid enthalpies, h_v and h_l, it is recalled that for thermally perfect species

$$h_l = \int_0^T C_{pl}\, dT', \quad h_v = \int_0^T C_{pv}\, dT' + h_v^0, \tag{2.23}$$

where the molar enthalpy of the mixture in continuous form is

$$h = (1 - X_v)C_{pga}T + X_v(C_{pv}T + h_v^0). \tag{2.24}$$

The reference enthalpy for the liquid and the carrier gas are taken to be null at $T = 0$, and a non-null reference value of the enthalpy of the vapor mixture, h_v^0, is required for

the vapor. To find h_v^0, its relation it to L_v is derived, having defined

$$\mathbf{J}L_v = \sum_{\alpha=1}^{N} \mathbf{J}_\alpha L_{v\alpha}, \tag{2.25}$$

where $\mathbf{J}$ is the total flux and $\mathbf{J}_\alpha = \mathbf{J}X_\alpha + \mathbf{J}_{D\alpha}$. For each component

$$L_{v\alpha} = h_{v\alpha}(T_s) - h_{l\alpha}(T_s) \tag{2.26}$$

where $h_{v\alpha}(T_s) = h_{v\alpha}^0 + \int_0^{T_s} C_{pv\alpha}(T')dT'$ and $h_{l\alpha}(T_s) = \int_0^{T_s} C_{pl\alpha}(T')dT'$.Substituting eq. 2.18 and those in Tamim & Hallett (1995) for $C_{pl}(\theta_l)$ and $L_v(T_s, \theta_{vs})$ in eq. 2.25, and integrating the right-hand side over all species, results to obtaining an equation with a single unknown, h_v^0, for which the equation is then solved. For example, according to Tamim & Hallett (1995), in discrete form, $L_v(m_\alpha) = A_h + B_h m_\alpha$, and the equivalent CT form is obtained by integrating over m_α to lead to

$$C_{pl} = \theta_l \left[A_l + B_l T_d + C_l T_d^2\right], \tag{2.27}$$

$$L_v(T_s) = \left[\frac{T_{cr} - T_s}{T_{cr} - T_b}\right]^{0.38} \times \left[A_h + B_h X_{vs}\theta_{vs} - \frac{B_h c\overline{D}}{J_{rs}}[\nabla(X_v\theta_v)]_{r,s}\right], \tag{2.28}$$

where A_l, B_l, C_l, A_h and B_h are constants listed in Tamim & Hallett (1995), $\theta_l = \int_0^\infty f_l(m_\alpha)m_\alpha dm_\alpha$ and the subscripts b and cr refer to the boiling point and to the critical point. Also, in discrete form, $T_{cr}(m_\alpha) = A_{cr} + B_{cr}m_\alpha$ and the equivalent CT form is obtained by integrating over m_α. For consistency with other correlations, it can be shown that a linear approximation of $h_v^0(m_\alpha) = Km_\alpha + K'$ can be made, and an equivalent CT expression is used in the calculation (see § 4.4.1). Since for a specified fuel h_v^0 is constant, it is evaluated at the reference temperature T_{wb}. To compute T_{wb}, an empirical correlation of experimental results is employed (see Miller *et al.* (1998))

$$T_{wb} = 137\left(\frac{T_b}{373.15}\right)^{0.68}\log_{10}(T_g) - 45, \tag{2.29}$$

where in discrete form $T_b(m_\alpha) = A_b + B_b m_\alpha$ and the equivalent CT expression is used in eq. 2.29; A_b and B_b are constants whose value is listed in Tamim & Hallett (1995).

The boundary conditions at the drop surface express the conservation of total (i.e. diffusive plus convective) molar mass, molar species and heat fluxes. To relate the fugacities on the two sides of the drop surface, Raoult's law is used, which for a mixture of discrete components is

$$X_{v\alpha} = X_{l\alpha}\left(p_{v\alpha}/p\right), \tag{2.30}$$

where $p_{v\alpha}$ is the α-species vapor pressure. In CT form, Raoult's law becomes

$$X_v = \int_{\gamma}^{\infty} f_l(m_\alpha)\frac{p_v}{p}dm_\alpha, \tag{2.31}$$

which weighted by m_α and $(m_\alpha - \theta_v)^2$ yields the vapor mean molar weight and the vapor variance in molecular weight at drop surface

$$(X_v\theta_v)_s = \int_{\gamma}^{\infty} f_l(m_\alpha)\frac{p_v(m_\alpha)}{p}m_\alpha dm_\alpha, \tag{2.32}$$

$$(X_v\sigma_v^2)_s = \int_{\gamma}^{\infty} f_l(m_\alpha)\frac{p_v(m_\alpha)}{p}\left(m_\alpha - \theta_v\right)^2 dm_\alpha. \tag{2.33}$$

The vapor pressure is given by the Clausius-Clapeyron equation in CT form

$$p_v(m_\alpha) = p_{atm}\exp\left[\left(\frac{\Delta s_{fg}}{R_u}\right)\left(1 - \frac{T_b(m_\alpha)}{T_s}\right)\right], \tag{2.34}$$

where $p_{atm} = 1$ atm and the entropy of vaporization Δs_{fg}, can be expressed using Trouton's empirical law $\Delta s_{fg} = L_v/T_b \simeq 87.9\ J\ K^{-1}mol^{-1}$. Using the relationships between θ, ζ, β and γ, and integrating eqs. 2.31 - 2.34 over m_α to obtain the CT form of the boundary conditions yields relationships between X_{vs} and the distribution parameters in the liquid, and between the distribution parameters in the liquid and vapor

$$X_{vs} = \frac{p_{atm}}{p_e}\frac{\exp\left[\Delta s_{fg}/\left(R_u T_s\right)\left(T_s - A_b - \gamma B_b\right)\right]}{\left(1 + \Delta s_{fg}/\left(R_u T_s\right)B_b\beta_l\right)^{\zeta_l}}, \tag{2.35}$$

$$\theta_{vs} - \gamma = \frac{\theta_l - \gamma}{1 + \dfrac{\left(\Delta s_{fg}/R_u\right)\left(1 - A_b/T_s\right)\left(B_b/\left(T_s - A_b\right)\right)\sigma_l^2}{\theta_l - \gamma}}, \tag{2.36}$$

$$\sigma_{vs}^2 = \sigma_l^2\left[\frac{\theta_{sv} - \gamma}{\theta_l - \gamma}\right]^2, \tag{2.37}$$

having assumed that $\gamma_l = \gamma_{vs} = \gamma$.

2.2. *Mixing layer conservation equations*

2.2.1. *Gas phase conservation equations*

The gas phase formulation of Miller & Bellan (1999) is here modified in three ways. First, two transport equations, for θ_v and ψ_v, are added to represent the entire molar weight range of evaporated fuel species; ψ_v is used as a dependent variable instead of the σ^2 (as in the drop model) because the resulting equation is simpler. Second, as in Okong'o & Bellan (2002a), the influence of the diffusion velocities are included in the heat flux vector because they were shown in Okong'o & Bellan (2002a) to be the dominant contribution, as conductive effects were relatively small in these simulations. Finally, since all available thermophysical property correlations (see Chou & Prausnitz (1986), Tamim & Hallett (1995)) utilize m_α, for consistency reasons two of the primitive variables are now c and X_α instead of ρ and the mass fractions, $Y_\alpha = X_\alpha m_\alpha / m$.

- *Continuity*

$$\frac{\partial \rho}{\partial t} + \frac{\partial}{\partial x_j}\left[\rho u_j\right] = S_{I\text{-mass}}, \tag{2.38}$$

where j denotes the Cartesian coordinate, $\mathbf{u}$ is the velocity of the mean mass and $S_{I\text{-mass}}$ is the mass source due to evaporation. This leads to an equation for c

$$\frac{\partial c}{\partial t} + \frac{\partial}{\partial x_j}\left[c u_j\right] = -\frac{c}{m}\frac{Dm}{Dt} + \frac{S_{I\text{-mass}}}{m}. \tag{2.39}$$

Further manipulation of eq. 2.39 with the mean molar weight equation (developed below) yields

$$\frac{\partial c}{\partial t} + \frac{\partial}{\partial x_j}\left[c u_j\right] = \frac{\partial}{\partial x_j}[c\overline{D}\frac{\partial}{\partial x_j}\left(X_v\right)] - \frac{1}{m_{ga}}\frac{\partial}{\partial x_j}[c\widetilde{D}\frac{\partial}{\partial x_j}\left(X_v\theta_v\right)] + S_{I\text{-mole}} \tag{2.40}$$

where $S_{I\text{-mole}}$ is the molar source due to evaporation.

- *Momentum conservation*

$$\frac{\partial(\rho u_i)}{\partial t} + \frac{\partial}{\partial x_j}\left[\rho u_i u_j + p\delta_{ij} - \tau_{ij}\right] = S_{II,j} \tag{2.41}$$

where τ_{ij} is the stress tensor

$$\tau_{ij} = \mu\left[2S_{ij} - (2/3)S_{kk}\delta_{ij}\right], \qquad S_{ij} = (1/2)(\partial u_i/\partial x_j + \partial u_j/\partial x_i), \tag{2.42}$$

with δ_{ij} being the Kronecker delta function, and $\mathbf{S}_{II}$ is the momentum source due to the drop-gas interaction.

- *Energy conservation*

$$\frac{\partial(ce_t)}{\partial t} + \frac{\partial}{\partial x_j}\left[(ce_t + p)\,u_j - \lambda\frac{\partial T}{\partial x_j} - u_i\tau_{ij}\right] + \frac{\partial}{\partial x_j}\left[\sum_{\beta=[ga,[1,N]]} J_{Dj\beta}h_\beta\right] = S_{III} \tag{2.43}$$

where S_{III} is the source term due to the drop/gas interaction and

$$\sum_{\beta=[ga,[1,N]]} J_{Dj\beta}h_\beta = -\{\int_0^\infty cD(m_\alpha)\frac{\partial[X_v f_v(m_\alpha)]}{\partial x_j}\times\left(h_v^0(m_\alpha) + C_{pv}(m_\alpha)T\right)\cdot dm_\alpha\} + J_{Djga}C_{pga}T. \tag{2.44}$$

Since $\sum_{\beta=[ga,[1,N]]} m_\beta \mathbf{J}_{D\beta} = 0$, it follows that

$$J_{Djga} = \frac{1}{m_{ga}}\int_0^\infty cmD(m_\alpha)\frac{\partial[X_v f_v(m_\alpha)]}{\partial x_j}\,dm_\alpha, \tag{2.45}$$

leading to

$$\sum_{\beta=[ga,[1,N]]} J_{Dj\beta}h_\beta = -\left(K' + R_u A_c T\right)c\overline{D}\frac{\partial X_v}{\partial x_j} - \left(K + R_u B_c T - \frac{C_{pga}T}{m_{ga}}\right)c\widetilde{D}\frac{\partial[X_v\theta_v]}{\partial x_j}. \tag{2.46}$$

- *Species conservation*

The discrete form of the conservation equation for the partial species density is

$$\frac{\partial(\rho Y_\alpha)}{\partial t} + \frac{\partial(\rho Y_\alpha u_j)}{\partial x_j} = \frac{\partial}{\partial x_j}\left(\rho D_\alpha\frac{\partial Y_\alpha}{\partial x_j}\right) + S_{I\alpha\text{-mass}} \tag{2.47}$$

where $S_{I\alpha\text{-mass}}$ is the evaporated mass of α-species from the drop; $S_{I\text{-mass}} = \sum_{\alpha=1}^{N} S_{I\alpha\text{-mass}}$.

Following the same protocol and assumptions as for the single drop, in CT form this

equation becomes

$$\frac{\partial(cX_v)}{\partial t} + \frac{\partial}{\partial x_j}\left(cX_v u_j - c\overline{D}\frac{\partial X_v}{\partial x_j}\right) = S_{I\text{-mole}}. \tag{2.48}$$

- *Vapor mean-molar-weight transport equation*

Integrating eq. 2.47 over dm_α and using the assumptions of Tamim & Hallett (1995) yields

$$\frac{\partial(cX_v\theta_v)}{\partial t} + \frac{\partial}{\partial x_j}\left[cX_v\theta_v u_j - c\widetilde{D}\frac{\partial(X_v\theta_v)}{\partial x_j}\right] = S_{I\text{-mass}}. \tag{2.49}$$

- *Second moment transport equation*

Multiplying eq. 2.47 by m_α and integrating it over dm_α leads to

$$\frac{\partial(cX_v\psi_v)}{\partial t} + \frac{\partial}{\partial x_j}\left[cX_v\psi_v u_j - c\widehat{D}\frac{\partial(X_v\psi_v)}{\partial x_j}\right] = S_\psi \tag{2.50}$$

where S_ψ is the source of $cX_v\psi_v$ in the gas phase due to drop evaporation.

- *Equation of state*

The perfect gas equation of state, $p = cR_uT$, is used to close the system of gas-phase equations.

2.2.2. *Individual drop governing equations*

Coupled to the gas-phase conservation equations, the drop equations for the position, $\boldsymbol{\chi}$, the velocity, $\mathbf{v}$, T_d, θ_l and ψ_l are

$$\begin{aligned}
\frac{d\chi_i}{dt} &= v_i, \\
\frac{dv_i}{dt} &= \frac{F_i}{M_d}, \\
\frac{dT_d}{dt} &= \frac{Q + (d\mathcal{N}/dt)L_v}{\mathcal{N}C_l}, \\
\frac{d\theta_l}{dt} &= \frac{6J_{rs}}{c_l d}\left[\theta_l + \frac{\theta_v X_v - \theta_{vs}X_{vs}(1+B)}{B}\right], \\
\frac{d\psi_l}{dt} &= \frac{6J_{rs}}{c_l d}\left[\psi_l + \frac{\psi_v X_v - \psi_{vs}X_{vs}(1+B)}{B}\right],
\end{aligned} \tag{2.51}$$

where according to Hallett (2000)

$$J_{rs} = \frac{c\overline{D}}{d/2}\ln(1+B) \quad \text{with } B = \frac{X_{vs} - X_v}{1 - X_{vs}} \tag{2.52}$$

where B is the CT equivalent of the Spalding transfer number (Williams (1965)). The force term, F_i, the heat transfer term, Q, and the enthalpy associated with the evaporation $L_v(d\mathcal{N}/dt)$ account for the coupling between the gas and the drops. The values of the gas-phase variables $(u_i, T, X_v, \theta_v, \psi_v)$ at each droplet location serve now as the far field boundary conditions for the single-drop equations presented above. Using the validated models for F_i, Q and $d\mathcal{N}/dt$ described in Miller *et al.* (1998) and in Hallett (2000), one obtains

$$\begin{aligned} F_j &= \left(\frac{M_d}{\tau_d}\right) f_1 (u_j - v_j) \\ Q &= \left(\frac{M_d}{\tau_d}\right) \frac{Nu\ C_{pg}}{3\,\mathrm{Pr}\ m} f_2 (T_g - T_d) \\ \frac{d\mathcal{N}}{dt} &= J_{rs}\frac{\pi d^2}{4} = -\left(\frac{M_d}{\tau_d}\right)\frac{Sh}{3Sc\,m}\ln(1+B) \end{aligned} \tag{2.53}$$

where $\tau_d = \rho_l d^2/(18\mu)$ is the particle time constant for Stokes flow, and μ is the viscosity of the carrier gas; $\mathrm{Pr} = \mu C_{pg}/(\lambda m)$ and $Sc = \mu/(\rho\overline{D})$ are the Prandtl and the Schmidt numbers respectively. The Nusselt, Nu, and the Sherwood, Sh, numbers are semi-empirically modified using the Ranz-Marshall correlations to account for convective effects in the heat and the mass transfer (see the detailed relationships in Miller & Bellan (1999)). f_1 is an empirical correction to Stokes drag accounting for both finite droplet Reynolds numbers ($\mathrm{Re}_d = \rho \parallel \mathbf{u} - \mathbf{v} \parallel d/\mu$) and a Reynolds number based on the blowing velocity ($\mathrm{Re}_b = \rho U_b d/\mu$, with $U_b = J_{rs}/c$) due to evaporation; the exact relationship for f_1 is listed in Miller & Bellan (1999). f_2 is an analytical correction to heat transfer due to evaporation

$$f_2 = \frac{\kappa}{\exp(\kappa) - 1}, \quad \kappa = -1.5\,\mathrm{Pr}\ \tau_d \frac{1}{\mathcal{N}}\frac{d\mathcal{N}}{dt}. \tag{2.54}$$

Finally, μ is computed from the specified initial (subscript 0) Reynolds number, Re_0,

$$\mu = \rho \Delta U_0 \delta_{\omega,0} / \mathrm{Re}_0, \tag{2.55}$$

where $\Delta U_0 = 2U_0$ is the initial difference in the freestream velocities calculated from the specified initial Mach number, $M_{c,0}$ (see details in Miller & Bellan (1999)), and $\delta_{\omega,0}$ is the initial vorticity thickness. The specification of Pr, Sc and Re_0 leads to a family of gas-phase solutions that is independent of the actual values of μ, λ and $\overline{D}$; this is the principle of flow similarity lucidly stated by Batchelor (1967). However, the drop characteristic time τ_d depends explicitly on μ, meaning that the μ magnitude will influence the drop interaction with the flow. The choice of the $\tau_d(\mu)$ value is intended to render the drop and flow characteristic times of same order of magnitude so as to enable the investigation of their interaction.

2.2.3. *Source terms*

The source terms in eqs. 2.40, 2.41, 2.43, 2.48 - 2.50 express the phase coupling of molar mass, momentum, energy, mean molar weight and second moment of the distribution function. Using conservation principles, one obtains

$$S_{I\text{-mass}} = -\sum_{q=1}^{N_d} \frac{w_q}{\Delta x^3} \left[\frac{d(\mathcal{N}\theta_l)}{dt} \right]_q, \tag{2.56}$$

$$S_{I\text{-mole}} = -\sum_{q=1}^{N_d} \frac{w_q}{\Delta x^3} \left[\frac{d\mathcal{N}}{dt} \right]_q, \tag{2.57}$$

$$S_{II,j} = -\sum_{q=1}^{N_d} \frac{w_q}{\Delta x^3} \left[F_j + \frac{d(\mathcal{N}\theta_l)}{dt} v_j \right]_q, \tag{2.58}$$

$$S_{III} = -\sum_{q=1}^{N_d} \frac{w_q}{\Delta x^3} \left[v_j F_j + Q + \frac{d\mathcal{N}}{dt} \left(\frac{\theta_l v_j v_j}{2} + h_{v,s} \right) \right]_q, \tag{2.59}$$

$$S_{\psi} = -\sum_{q=1}^{N_d} \frac{w_q}{\Delta x^3} \left[\frac{d(\mathcal{N}\psi_l)}{dt} \right]_q \tag{2.60}$$

where the summations are over all drops residing within a local numerical discretization volume, Δx^3, and a geometrical weighting factor w_q is used to distribute the individual

drop contributions to the nearest eight grid points in proportion to their distance from the drop location (see Miller & Bellan (1999)). $h_{v,s} = C_l T_s + L_v$ is the enthalpy of the evaporated species.

3. Single drop results

Before undertaking DNS of the mixing layer with MC-fuel drops it is important to assess the ability of the CT method to portray a variety of fuel mixtures. In this spirit, since validated single SC-fuel drop models do exist (Miller *et al.* (1998)), those results are compared with results from simulations using a sharply-peaked distribution f. Further, single, isolated MC-fuel drop simulations were conducted to explore the novel possibilities of the CT formulation.

All single, isolated drop results were found by solving eqs. 2.20 - 2.22 and 2.52 in which X_v is replaced by X_{ve} to account for the specified far field conditions. These equations were solved in conjunction with the boundary conditions of eqs. 2.35 - 2.37 using a finite difference time discretization with a time step of $10^{-6}s$. In the MC simulations, all transport properties (including λ whose dependency on these variables is listed in Tamim & Hallett (1995)) were functions of θ and T as stated above.

3.1. *Sharply peaked distribution versus SC-fuel representation*

Displayed in Fig. 1 are results obtained from several drop models exercised for the same initial conditions: $T_{ge} = 1000K$, $T_{d,0} = 300K, d_0 = 2 \times 10^{-3}m, \mathrm{Re}_{d,0} = 17$. Model 1 is the rapid mixing model (i.e. the infinite λ_l limit) without evaporative correction to heat transfer as in Chen & Pereira (1996) (i.e. $f_2 = 1$); Model 2 is the rapid mixing model with an evaporative correction to heat and mass transfer as in Abramzon & Sirignano (1989); Model 3 is based on the heat-mass analogy and like Model 2 takes into account the heating period of the droplet; and Model 4 additionally incorporates the non-equilibrium

evaporation law based on the Langmuir-Knudsen (LK) law. All these models have been discussed in detail in Miller *et al.* (1998) and they are here exercised for $n-$decane. The MC model is implemented with $\theta_{l,0} = 142\ kg/kmole$ to duplicate the molar weight of $n-$decane, $\sigma^2_{l,0} = 2\ (kg/kmole)^2$ to have a very sharply peaked distribution, and $\gamma_{l,0} = 138\ kg/kmole$ to restrict the molar weight of components to be close to $n-$decane. The thermophysical properties used in the calculations for $n-$decane are those listed in Miller *et al.* (1998).

Except for the heating period, the evaporation model using CT is closest to Model 4 (both d and T_d evolution) and is in better agreement with it than most of the other models, which are typically employed in two-phase flow simulations with evaporating drops. This agreement is significant since the Model 4 results were those found closest to experimental observations in Miller *et al.* (1998). The slight difference in the heating period between Model 4 and the CT model is attributed to the corresponding difference in fuel composition between the MC fuel and $n-$decane, which is reflected in the thermophysical properties. We also note that LK effects are insignificant for the drop size used in this calculation, and thus are not expected to influence the results (Model 4 includes LK effects, whereas the CT-based model does not). Based on the comparison presented in Fig. 1, the CT model seems to combine quantitative accuracy (given the difference in composition between the constant SC molar weight and the sharply peaked-f MC equivalent) with a more realistic description of the physics in the drop.

3.2. *Single MC-fuel drop results*

To establish the difference in baseline behavior between different MC fuels, several MC-fuel drop calculations were conducted. The parameters characterizing f for all the fuels used in the computations are listed in Table 1. The values of $\theta_{l,0}$ and $\sigma_{l,0}$ are prescribed,

whereas $\gamma_{l,0}$ is calculated from the condition that $T_{d,0} < T_{b,0}$ and therefore $\gamma_{l,0} = (T_{d,0} - A_b)/B_b$, meaning that it corresponds to the species having the lowest boiling point.

The results plotted in Fig. 2 are all for $T_{ge} = 1000$ K, $T_{d,0} = 300$ K, $\mathrm{Re}_{d,0} = 0$ and $d_0 = 10^{-4}m$. For diesel, which is the least volatile fuel, an enlarged heating period is necessary before initiating vaporization, and thus the drop lifetime (Fig. 2a) is largest. The heating period of gasoline is slightly shorter than that of $n-$decane because the lighter species in gasoline are more volatile, however, as the heavier species begin evaporating, the drop evaporation rate decreases with respect to n-decane. Illustrated in Fig. 2b is the time evolution of T_d for the $n-$decane and diesel-fuel drops, as well as T_b for the diesel-fuel drop. In both situations, T_d is bounded by T_b; for n-decane, an asymptotic T_d behavior is reached, however, no such situation occurs for the diesel drop whose T_b evolves with the composition. Comparing the initial diesel-fuel drop composition with that at half through the drop lifetime (see Fig. 2c), one discerns the disappearance of the lighter molar weight species, which are well known to be more volatile, and the concomitant larger peak at a larger molar weight. To further quantify the diesel-fuel drop evolution, the surface vapor mole fraction is displayed in Fig. 2d as a function of t. Following the initial transient during which X_{vs} continuously increases, a stationary state is reached corresponding to a quasi-steady evaporation. In the remaining part of the study we will explore the impact that the different evolution of MC-fuel drops versus SC-fuel drops has on the characteristics of drop-laden mixing layers.

4. Mixing layer results

To explore the approximations introduced by the SC assumption, DNS of SC- and MC-fuel drop-laden mixing layers are compared for the same conditions except for the identity of the fuel in the drops. The present simulations using diesel fuel are compared

with those of Okong'o & Bellan (2002a) using $n-$decane (a common simulant of diesel fuel).

4.1. *Numerical procedure, initial and boundary conditions*

Figure 3 shows the computational domain configuration and the definition of the streamwise, x_1, cross-stream, x_2, and spanwise, x_3, coordinates with lengths $L_1 = 4\lambda_1 = 29.16\delta_{\omega,0}$, $L_2 = 1.1L_1$, and $L_3 = 4\lambda_3 = 0.6L_1$, with $L_1 = 0.2m$. The parameters λ_1 and λ_3 are forcing wavelengths in the x_1 and x_3 directions, and were used to excite the layer in order to induce roll-up and pairing as in Moser & Rogers (1991), Miller & Bellan (1999) and Miller & Bellan (2000). $\delta_{\omega,0} = \Delta U_0 / < \partial u_1/\partial x_2 >$ where the brackets $<$ $>$ indicate averaging over homogeneous (x_1, x_3) planes, and the initial condition for u_1 is detailed in Miller & Bellan (1999); for this initial condition $\delta_{\omega,0} = 6.85 \times 10^{-3}m$. The drops were distributed randomly throughout the lower stream with uniform number density and a uniform temperature. The initial drop slip velocity with respect to the gas was null, and the initial drop-size distribution was polydisperse and specified by the Stokes number, $St = \tau_d \Delta U_0/\delta_{\omega,0}$ (both $< St_0 >$ and $St_{0,RMS}$). Table 2 summarizes the initial conditions, where the SC mixing layer results represent the database originated by Okong'o & Bellan (2002a). Owing to the larger ρ_l, at same initial St, the MC calculations are initialized with a larger number of drops, $N_{d,0}$, and a smaller $< d_0 >$ than their SC counterpart. For all simulations, the initial mass fraction of the evaporated species was null and in the MC simulations the initial molar weight was 137 kg/kmole in the entire domain. Re_0 was chosen small enough to obtain resolution of all scales. The mass loading, ML, is defined as the total mass of the liquid relative to the total mass of the gas in the laden stream. Furthermore, in all simulations $M_{c,0} = 0.35$ and $\mathrm{Pr} = Sc = 0.67$.

The numerical mesh used in the simulations was uniform in all directions and is listed in the caption of Table 2. The boundary conditions in the x_1 and x_3 directions were

periodic and the adiabatic slip-wall conditions in the x_2 direction previously derived by Poinsot & Lele (1992) and Baum *et al.* (1994), based on the wave decomposition method, were here adapted to the CT model for MC mixtures (see Appendix A).

The governing equations were solved numerically using a fourth-order explicit Runge-Kutta temporal integration for all time derivatives and eight-order central finite differences for all spatial derivatives. A fourth-order Lagrange interpolation procedure was used to obtain gas-phase variable values at drop locations. As drops evaporate, their residual mass decreases. Drops whose residual mass was less than 3% were removed from the calculation. The initial conditions for the temporally developing mixing layer configuration were based on those of Moser & Rogers (1991) and were detailed in Miller & Bellan (1999).

One computational difficulty in performing mixing layer MC-fuel drop simulations is the determination of parameters K and $K^{'}$ in the CT form of $h_v^0(m_\alpha)$, $h_v^0(\theta_v) = \int_0^\infty h_v^0(m_\alpha) f_v(m_\alpha) dm_\alpha = K\theta_v + K'$. For an isolated MC-fuel drop whose far field conditions are specified, eq. ?? becomes

$$L_v(T_{wb}) = \underbrace{K\frac{X_{vs}\theta_{vs}(1+B) - X_{ve}\theta_{ve}}{B} + K'}_{\text{reference enthalpy } h_v^0} + C_l T_{wb} - R_u T_{wb} A_c - R T_{wb} B_c \frac{X_{vs}\theta_{vs}(1+B) - X_{ve}\theta_{ve}}{B}. \tag{4.1}$$

Therefore $K^{'}$ can be obtained from eq. 4.1 at the initial condition, and K can be found as a function of θ_{vs}. Although in principle the same procedure can be applied for the mixing layer drops whose far field conditions change as a function of position and time, this calculation introduces a large computational overhead. To remove this computational overhead, single, isolated drop computations were performed for diesel-fuel at several initial conditions, and the values of K and $K^{'}$ were empirically determined (as the composition of the drop changed with time) from a plot of h_v^0 versus θ_{vs} created according to eq.

4.1.While it is apparent that h_v^0 is not strictly linear and depends on the initial conditions, for ease of computation in the mixing layer simulations, the linear relationship for h_v^0 was retained, with the following values $K = -100,175\ J/kg$, $K' = 119,663,800\ J/kmole$. Although the linear relationship is only qualitatively correct, it embodies the general behavior exhibited in these calculations and it is thus deemed appropriate considering the uncertainty associated with the thermophysical parameters for MC-fuel distributions.

All transport properties were calculated at 350 K for all simulations.

4.2. *Global layer evolution and transition attainment*

To compare SC and MC simulations, the global evolution of the layers through the momentum thickness, δ_m

$$\delta_m = \frac{1}{(\theta_1 - \theta_2)^2} \int_{-L_{2,\min}}^{L_{2,\max}} -(\theta_2 + < \rho u_1 >)(\theta_1 + < \rho u_1 >) dx_2 \tag{4.2}$$

was first examined, with $\theta_1 =< \rho u_1 >_{x_2 = L_{2,\max}}$ and $\theta_2 =< \rho u_1 >_{x_2 = -L_{2,\min}}$, $L_{2,\max} = -L_2/2$ and $L_{2,\min} = L_2/2$. Illustrated in Fig. 4a is $\delta_m/\delta_{\omega,0}$ as a function of $t^* = t\Delta U_0/\delta_{\omega,0}$ for both SC-fuel and MC-fuel drop-laden layers. All layers display roll-up and a double pairing, with a plateau after the first pairing indicative of the forcing effect. At same ML_0 one discerns little difference between the SC and MC layer growth, with the SC layers growing somewhat larger before the first pairing and vice versa after the second pairing. The larger ML_0 layers exhibit a smaller and more linear growth with lesser influence from the forcing, this being attributed to the higher density stratification between the two streams resulting in more difficulty to entrain. The SC5 layer displays the smallest ultimate growth, with the smallest momentum-thickness-based Reynolds number, $\mathrm{Re}_m \equiv \mathrm{Re}_0\, \delta_m/\delta_{\omega,0}$, at transition (1415 for SC2, 1450 for MC2, 1360 for SC5, and 1465 for MC5). The larger Re_m at transition for MC-fuel simulations compared to

their SC counterpart indicates that these former layers may have enhanced turbulent features compared to the latter.

Owing to the major role of vorticity, $\boldsymbol{\omega} \equiv \nabla \times \mathbf{u}$, in turbulent flows, global aspects of the flow that are associated with $\boldsymbol{\omega}$ were also examined. In Figs. 4a and 4c the volume averaged non-dimensional positive spanwise vorticity, $<< \omega_3^+ >> \delta_{\omega,0}/\Delta U_0$, and the non-dimensional enstrophy, $<< \omega_i\omega_i >> (\delta_{\omega,0}/\Delta U_0)^2$, evolutions are depicted as functions of t^*; here $<<>>$ denotes volume averaging. The positive spanwise vorticity (Fig. 4b) begins increasing after roll-up, and following the plateau displayed after the first pairing, continues to increase at a sustained rate. Although the SC5 layer initially follows the growth of the $ML_0 = 0.2$ layers, it eventually reaches the highest peak, indicating that the increased number of drops contribute to an increased formation of small scales. With respect to the other three layers, the MC5 layer has a delayed growth and peak (see Table 2 for the peak times), which is however still larger than that of both $ML_0 = 0.2$ layers, albeit slightly smaller than that of the SC5 layer. The indications are that the MC layers achieve a slightly reduced small-scale formation than their SC counterpart. A similar behavior to that of ω_3^+ is portrayed in Fig. 4c for the enstrophy, but we note that these indications pertain only to the attained maxima and are reversed past the culminating point of the curves. With increasing ML_0, the difference in enstrophy evolution between the SC and MC layers becomes enhanced, with the MC5 layer evolving in a more linear manner, lagging in stretching and tilting activity, and displaying a delayed peak with respect to the other layers, although all layers reach similar enstrophy levels. To understand the relatively small sensitivity to the fuel composition, the $\boldsymbol{\omega}$ and $\boldsymbol{\omega} \cdot \boldsymbol{\omega}$ equations were derived and their budget was evaluated (not shown). The largest contribution to vorticity production is from the stretching and tilting term followed by the viscous term, while the source terms have negligible contributions. Therefore, the small sensitivity of

the global vorticity aspects to the fuel composition may be traced to the negligible role of the source terms for these values of ML_0. However, one discerns a generally higher activity in the voticity-magnitude RMS and an enhanced effect of viscosity in the ω_3 RMS for the SC-fuel drop-laden layer.

By our stringent criterion of mixing transition achievement, not only $\delta_m/\delta_{\omega,0}, << \omega_3^+ >> \delta_{\omega,0}/\Delta U_0$ and $<< \omega_i\omega_i >> (\delta_{\omega,0}/\Delta U_0)^2$ must increase sharply and in a sustained manner, but also the spectra must be smooth, indicative of the full range of scales characteristic of turbulence. Illustrated as an example, Fig 5 plots represent the spanwise spectra for the MC5 simulation at the time identified in Table 2 as corresponding to mixing transition. These plots display the full range of scales indicative of transition. The peak in the energy spectra at a wavenumber of 4 is attributed to the spanwise forcing. The plots additionally show that the flow is completely resolved, as most of the energy is in the high wavenumber regime and there is no energy accumulation in the low wavenumbers.

4.3. *Flow characteristics and drop organization at transition*

Since in combustion applications the local variables govern the reaction rates, it is pertinent to examine the local vorticity, drop number distribution and the evaporated-fuel mass fraction.

4.3.1. *Vorticity and helicity*

Comparison of contour plots of ω_3 for SC2 and MC2 after the second pairing ($t^* = 87$) show a markedly different local structure (not shown). The maximum ω_3^+ is smaller for the MC-fuel drop-laden layer, indicating that a wide spread molar-weight liquid-fuel composition may globally impede vorticity production; this conclusion is consistent with the vorticity and vorticity-magnitude budget analyses. Although the general level

of vorticity activity is higher in the SC-fuel layer, locally one observes considerably more numerous high vorticity regions for the MC-fuel mixing layer. These sites of very high vorticity lead to a more highly structured flow (not shown) by inducing the formation of high drop number density regions through flinging the drops away from the high to the low vorticity locations. Since transition is attained following the ω_3^+ peak, the vorticity level is reduced from that at $t^* = 87$, however the SC-fuel layers retain larger ω_3^+ with respect to the MC-fuel layers. Figure 6 shows ω_3 in the between-the-braid plane for the SC (Fig. 6a and 6b) and MC (Fig. 6c and 6d) layers at transition; the braid plane plots display a similar behavior. Numerous sites of positive spanwise vorticity, plotted in solid lines, are obvious in all figures, indicating small-scale production. Although the major visual features of the flow are similar for SC2 and MC2 simulations, the details remain different. Noteworthy, the MC2 layer exhibits a more spotty aspect with isolated localities of high vorticity. As ML_0 increases, the ratio of the maximum positive spanwise vorticity level between SC and MC simulations becomes larger and it becomes easier to discern the more numerous regions of high vorticity for the MC-fuel layer.

Because helicity describes the topology, and more precisely measures the knottedness, of the flow it can be an important diagnostic in the analysis of turbulence features. Such analyses were performed by Moffatt (1969), André & Lesieur (1977), Moffatt (1985), Pelz *et al.* (1985), Shtilman *et al.* (1985), Pelz *et al.* (1986), Rogers & Moin (1987), Shtilman *et al.* (1988) and Moffatt (1992), and Wallace *et al.* (1992) studied helicity experimentally. For two-phase flows with phase change, the helicity-density equation is

$$\begin{aligned}\frac{D}{Dt}(\mathbf{u}\cdot\boldsymbol{\omega}) = {} & \mathbf{u}\cdot(\boldsymbol{\omega}\cdot\nabla\mathbf{u}) - \mathbf{u}\cdot\boldsymbol{\omega}\,(\nabla\cdot\mathbf{u}) - \mathbf{u}\cdot\left(\nabla\left(\frac{1}{\rho}\right)\times\nabla p\right) - \frac{1}{\rho}\boldsymbol{\omega}\cdot\nabla p \\ & + \mathbf{u}\cdot\left(\nabla\times\left(\frac{1}{\rho}\nabla\cdot\tau\right)\right) + \frac{1}{\rho}\boldsymbol{\omega}\cdot(\nabla\cdot\tau) \\ & + \mathbf{u}\cdot\left(\nabla\times\left(\frac{1}{\rho}\mathbf{S}_{II}\right)\right) + \frac{1}{\rho}\boldsymbol{\omega}\cdot\mathbf{S}_{II} - \mathbf{u}\cdot\left(\nabla\times\left(\frac{1}{\rho}\mathbf{u}S_I\right)\right) - \frac{1}{\rho}\boldsymbol{\omega}\cdot\mathbf{u}S_I\end{aligned} \tag{4.3}$$

where the terms on the last line originate from momentum and mass sources. Homogeneous (x_1, x_3)-plane averages were calculated to assess the helicity-density budget for the four simulations listed in Table 2. The results show that both the average (not shown) and the RMS (see Fig. 9) are dominated by the stretching/tilting term, by the scalar product of the vorticity with the pressure-gradient term, and by viscous effects (the viscous effects are overwhelmingly from $(1/\rho)\boldsymbol{\omega} \cdot (\nabla \cdot \tau)$, with the other term being negligible; not shown). The dilatation, baroclininc and source terms are all negligible, although with increased ML_0 the momentum-source terms become more important, as expected. Concomitant with the increase in the momentum-source-term contribution with increasing ML_0, all dynamic (i.e. non-source term) RMS contributions to the helicity-density decrease, indicating that there may be an ML_0 threshold at which source terms may become comparable to the other contributions or even dominate helicity-density production. Independent of ML_0, each of the dominating helicity-density contributions is larger for SC-fuel than for MC-fuel simulations, showing that fuel composition affects the dynamic features of the layer, albeit in an indirect manner. Comparing the relative aport of the dominant contributions for each simulation, the scalar product of the vorticity with the pressure-gradient term becomes larger for each of the MC simulations compared to its SC counterpart, indicating that the knottedness of the flow due to this effect becomes relatively more important for MC situations.

Because SC layers have regions of larger vorticity magnitude and helicity-density RMS at transition, these results do not support the indication from the global analysis that MC layers may have more turbulence activity than SC ones. However, MC layers display more small-scale structure than their SC equivalent, an aspect confirmed by the examination of the drop organization presented below.

4.3.2. *Drop organization*

As discussed above, MC calculations are initiated with larger N_d than their SC equivalent. Therefore, the pertinent quantity to examine is not N_d but the drop-number density, ρ_n. Visualizations of ρ_n, calculated as an Eulerian field from the instantaneous Lagrangian droplet locations

$$\rho_n = \sum_{q=1}^{N_d} \frac{w_q}{\Delta x^3}, \tag{4.4}$$

show the relationship between the regions of high vorticity and relatively small ρ_n. The results presented in Figs. 7a through 7d are at transition and qualitatively agree with those of Squires & Eaton (1991) who found that particles with a density larger than that of the carrier flow concentrate in regions of low vorticity and high strain. They are also reminiscent of the 'focusing' effect discussed by Crowe *et al.* (1988) for coherent vortices in the laminar flow context, however, they now occur at the small scale. The noteworthy feature in Fig. 7 is the small-scale structure formed, with drops profiling the small-scale vortices. The highest drop concentration (3.43×10^{10} for SC2, 3.16×10^{10} for MC2, 4.6×10^{10} for SC5 and 6.0×10^{10} for MC5, all in m^{-3}; these maxima are not necessarily shown on Fig.7 because they occur at point-wise locations and cannot be captured by a color rendering scale representative of the important features) is not at the periphery of the coherent vortex representing the ultimate structure resulting from the two pairings of the four initial vortices, but rather at the periphery of small-scale vortical structures. Following the second pairing, at $t^* = 87$, ρ_n exhibits considerably larger levels and displays much more structure for the MC2 than for the SC2 simulation (not shown). The smaller ρ_n is attributed to the faster drop evaporation (see § 4.4.1) inducing some drops to be completely evaporated and thus removed from the computation; whereas none of the drops in the MC2 simulation satisfy the criterion for complete evaporation. The larger ρ_n may also be attributable to the larger $N_{d,0}$ in MC computations. Comparing

ρ_n for the SC2 and MC2 simulations at transition (Figs. 7a and 7c), it appears that this evidence of higher maximum ρ_n for the MC2 simulation accompanied by an increased small-scale structure is lost, indicating drop re-organization. Except for more numerous locations of high ρ_n indicative of an increased structure for the MC5 compared to the SC5 simulation (compare Figs. 7b and 7d), it is similarly difficult to quantify from simple visual examination the differences between the two sets of results. The molar weight distribution depicted in Figs. 7e and 7f is illustrated in Fig. 7 for the purpose of direct visual comparisons with Figs. 7c and 7d and is discussed in detail in § 4.3.3.

To quantify the drop structure in the flow, we calculated the drop-number density conditionally averaged on the second invariant of the deformation tensor for compressible flow

$$II_u = -\frac{1}{2}\left[(S_{ij}S_{ij} - S_{kk}S_{ll}) - \frac{1}{2}\omega_i\omega_i\right] \tag{4.5}$$

and on a passive scalar ϕ (here the fuel mass fraction) which is chosen as $\phi < 0.5$ to ensure that primarily only laden-stream fluid is considered. The form of II_u is conducive to distinguishing portions of the flow that are of rotational or compressible nature, corresponding to $II_u > 0$, from other portions of the flow where strain dominate, corresponding to $II_u < 0$. Noteworthy, because the rotational part is weighted by 1/4 whereas the strain/compressibility part is weighted by 1/2, conditioning on II_u does not give an accurate portrayal of the relative ρ_n in these regions; to obtain an accurate proportion one would have to weigh appropriately the positive and negative contributions. However, this subtlety does not intervene if the intent is to compare the results from different simulations. Displayed in Fig. 8 are the non-dimensional conditional averages of ρ_n for all simulations listed in Table 2. Even with the uncertainties about comparing the ρ_n magnitude for positive and negative contributions, it is obvious that most drops accumulate first in regions where $II_u \simeq 0$, then in regions where $II_u < 0$ and finally at

locations where $II_u > 0$. On the scale of the plot, in the moderate and strongly positive II_u regions, ρ_n is merely a function of ML_0, with only subtle differences in regions of low vorticity and compressibility, where the SC simulations exhibit slightly larger values than their MC counterpart. However, larger differences between SC and MC results appear in the $II_u < 0$ regions. For $ML_0 = 0.2$ simulations, the plots in Fig. 8 show that with the exception of very strongly negative II_u regions, ρ_n is larger for MC2 than for SC2 in strain regions, indicating that ρ_n remains larger for MC2 past the second pairing and at transition. For $ML_0 = 0.5$ simulations, the results exhibit an even larger difference between the SC versus MC simulations, and in very strong strain regions, ρ_n is considerably larger for MC5 than for SC5. The highly non-monotonic variation of the MC plots in moderately to strongly $II_u < 0$ regions indicates an increased small-scale structure with respect to their SC equivalent. These quantitative results confirm the qualitative, visual observations from Figs. 7b and 7d and show that the MC-liquid composition impacts the ρ_n magnitude and its distribution. The reasons for this occurrence are discussed in § 4.4.

4.3.3. *Molar weight distribution for multicomponent-fuel simulations*

The distribution of gas-phase molar weight at transition is shown in Figs. 7e for MC2 and 7d for MC5 in the between-the-braid plane. Because of color rendering, the full range of molar weights was not possible to display (the maximum molar weight was 250 kg/kmole for MC2 and 212 kg/kmole for MC5), however, the deleted values in the upper range of molar weights occupy only point-like locations; for each of the two figures, the maximum shown molar weight was chosen based on the best color representation for the entire domain. Despite removing the largest values from the illustrations, the wide range of values and the very complex molar weight local distribution is noteworthy, which should be compared to the constant molar weight of n-decane, 142 kg/kmole, which is spatially distributed in the domain according to Y_v (see below). Most of the lighter

components, which egress from the drop earlier during evaporation, reside in the lower stream. The intermediary-weight components, which are released after the drops have been entrained, reside mostly in the interior of the layer as they have already participated in the mixing process. In contrast, the heavier components reside in the regions of high number density, as they evaporate later during the drop lifetime and have not participated in the mixing. Therefore, a segregation of chemical species becomes established according to the time when they were released from the drops. This segregation obviously cannot be captured by SC-fuel drop-laden mixing layer simulations.

In the between-the-braid plane, the MC5 layer encompasses more numerous high-molar-weight locations than the MC2 layer, consistent with the more numerous high ρ_n locations in the layer and with the larger maximum ρ_n. Also, the molar weight distribution is more inhomogeneous with increasing ML_0. In order to quantify the molar weight distribution across the layer at transition, (x_1, x_3)-plane average θ_v PDFs of the molar weight that are illustrative of the lower stream ($x_2/\delta_{\omega,0} = -12$), lower part of the layer ($x_2/\delta_{\omega,0} = -2.5$), and upper part of the layer ($x_2/\delta_{\omega,0} = 7$) were calculated. The PDF in the lower stream peaks at lower θ_v values and is akin to a delta function (not shown) culminating at lower θ_v-values with increasing ML_0 (156 kg/kmole for MC2 and 147 kg/kmole for MC5). The PDFs in the lower and upper parts of the layer are illustrated in Fig. 10. In the lower layer region the PDFs peak at higher values than in the lower stream and the peak location remains at smaller values with increasing ML_0. The small 'bumps' on each side of the peak correspond to regions of high ρ_n where high-molar-weight components reside. In the upper part of the layer, the PDFs widen in the higher θ_v range and their peak value decreases, with the higher peak now corresponding to the larger ML_0. The wider range is illustrative of the higher molar weight of components evaporated late in the drop lifetime and residing in the upper layer high-ρ_n region (e.g.

Figs. 7e and 7d). The small local peak evident in the low θ_v range represents a region of small molar weights traversed by the (x_1, x_3) plane at $x_2/\delta_{\omega,0} = 7$ (e.g. Fig. 7).

4.3.4. *Evaporated-fuel mass fraction*

The mass fraction of the evaporated species is illustrated in Fig. 11. Comparing the results from SC and MC simulations, it is apparent that the drops in the latter produce a smaller amount of vapor (see legends; the maxima, 0.096 for SC2, 0.1 for SC5, 0.067 for MC2 and 0.078 for MC5, are not displayed), which is attributed to the wide range of species volatility that leads to a decreasing evaporation rate once the most volatile components have been released. This behavior has already been identified in the single drop simulations discussed in § 3. Regions of larger Y_V generally correspond to the locations of high ρ_n, however, moderate Y_V regions are found throughout the layer owing to gas phase transport mechanisms that carry the evaporated species from the drop surface to other regions within the layer.

4.4. *First order statistics*

The first order statistics are calculated to enable a more complete understanding of the global and detailed features of the layers. For the drop variables, these statistics are Lagrangian, meaning that averages are performed on the ensemble of drops; we denote these averages by $\{\{\ \}\}$. The gas phase variables are subjected to Eulerian averages, meaning that they are performed over the volume and have been denoted by $<<\ >>$.

4.4.1. *Drop size*

Illustrated in Fig. 12a is the Lagrangian ensemble average of the residual drop diameter in the entire domain as a function of t^*; comparing non-dimensional rather than dimensional drop diameters removes the bias introduced by the smaller $< d_0 >$ in MC simulations. The linear behavior of the well-known d^2 - law is not observed in Fig. 12 as the

curves represent ensemble averages rather than the individual drop behavior. To understand the different fate of drops in the mixing layer (defined as $x_2/\delta_{\omega,0} \geqslant -7$) from those in the lower stream (i.e. $x_2/\delta_{\omega,0} < -7$), separate Lagrangian ensemble averages are depicted in Fig. 12b. For $ML_0 = 0.2$, the MC-fuel drops evaporate considerably slower than the SC-fuel drops (Fig. 12a) due to the decreased volatility accompanying the increase in molar weight. This decreased evaporation induces the drops to have more interaction with the flow, and this increased coupling results in the augmented small-scale structure discussed above. The evaporation rate is considerably reduced when $ML_0 = 0.5$. Also, although the MC5 evaporation rate is slower than that of SC5, the difference between the two simulations is considerably smaller than when $ML_0 = 0.2$. As stated earlier, the smaller evaporation rate of the MC simulations is attributed to the wide range of volatilities that reduces the evaporation once the most volatile components have been released; the smaller evaporation rate for $ML_0 = 0.5$ simulations is attributed to the larger number of drops, which represents a higher heat sink for the gas phase; finally, the reduced evaporation rate for the $ML_0 = 0.5$ simulations renders the individual-drop evaporation rate in each of those simulations more uniform in magnitude for reasons discussed in § 4.4.2. Comparisons of plots in Figs. 12a and 12b show that this general behavior is more typical of drops inside the layer. The drops in the lower stream reach an asymptotic size by the completion of the first pairing for $ML_0 = 0.2$ and by the end of roll-up for $ML_0 = 0.5$, indicating cessation of evaporation due to saturation. The earlier saturation for $ML_0 = 0.5$ is due to the higher initial ρ_n which induces a larger vapor accumulation in the lower stream.

To quantify the drop size at transition, displayed in Fig. 13 is the PDF of St in the mixing layer for the four simulations; since all variables are fixed in St except for d, the St value is indicative of the drop size. All four simulations were initiated with the

same St PDF (see Table 2), and therefore the differences exhibited in Fig. 13 are the result of either the ML_0 value, or the MC aspect. The probability of being at the mean is practically independent of ML_0 for the SC simulations and slightly reduced for MC5 compared to MC2; the mean drop size is reduced with decreasing ML_0 for each type of simulation indicative of enhanced evaporation. Independent of ML_0, the mean drop size is larger and the probability of being at the mean is higher for MC simulations compared to their SC counterpart. This observation is consistent with the narrower St distribution for each MC simulation compared to the equivalent SC one, indicating a decreased polydispersity resulting from the MC aspect.

The larger drop size and the reduced polydispersity for MC cases are attributed to the combination of slower evaporation with condensation (discussed in §4.4.2) which occurs in MC simulations, but does not occur in the SC case.

4.4.2. *Drop composition and temperature*

For SC computations, the drop composition is inherently invariant. In MC simulations, condensation occurs as the result of the drops being transported in regions of the flow having a different composition from their 'natural' far field defined as that corresponding to what would be obtained during single drop evaporation. The condensation of these species is clearly evident in Figs. 14a and 14c, where it is seen that although the mean molar weight increases with time due to the evaporation of the lighter components, the variance exhibits a non-monotonic behavior. Following an initial decrease due to the more volatile components leaving the liquid drop, $\{\{\sigma_l\}\}$ increases indicating that some mixture constituents that have already evaporated are now condensing back onto the drops; further variations in the variance indicate a slow, asymptotic evolution. This condensation process also contributes to the larger residual diameter of the MC-fuel drops observed in Figs. 12 and 13. The fate of the fuel composition for drops in different regions

of the layer was examined by performing separate ensemble averages over drops in the lower stream (i.e. for $x_2/\delta_{\omega,0} < -7$) and over drops in the mixing layer (defined here as the remaining of the domain). The results portrayed in Figs. 14b and 14d show that the lower stream drops reach relatively fast an asymptotic approximately-fixed composition, whereas the mixing-layer drops change composition, as both $\{\{\theta_l\}\}$ and $\{\{\sigma_l\}\}$ continue to vary. Whereas in the interior of the mixing layer $\{\{\theta_l\}\}$ increases with time, $\{\{\sigma_l\}\}$ exhibits a non-monotonic behavior indicative of concomitant evaporation of some species and condensation of other species. Thus, the MC-fuel drop diameter is the result of two competing instantaneous processes: evaporation and condensation.

The condensation also explains the variation in the drop temperature depicted in Fig. 15. The temperature of SC-fuel drops decreases initially due to evaporation. The further increase in $\{\{T_d\}\}$ is due to drop heating as a result of heat transfer from the gas phase. This stage is followed by a reduction in $\{\{T_d\}\}$ corresponding to a stronger evaporation induced by the larger drop temperature. Therefore evaporation and heating combine to render $\{\{T_d\}\}$ mildly periodic for the SC case. In contrast to the SC situation, the temperature of MC-fuel drops decreases for a much shorter time following the initial conditions, corresponding to the evaporation of the very light components. Following this stage, the drop temperature must increase before the heavier components leave the liquid, slowing down evaporation (see Fig. 12). When condensation is initiated (see Fig. 14), the drop temperature increases but this augmentation occurs at a smaller rate since the condensing vapor carries the higher temperature of the gas, thus facilitating evaporation of other components in the drop. Eventually, the condensation rate decreases and the drop temperature is high enough to allow a stronger evaporation, explaining the further decrease in $\{\{T_d\}\}$. Following the evaporation of these intermediary molar weight species, $\{\{T_d\}\}$ must again increase before the higher molar weight components

may evaporate. Thus, the MC-fuel drop temperature also has a periodic behavior, but at a larger average temperature than the SC-fuel drops. Figure 15 also shows that $\{\{T_d\}\}$ slightly increases with increasing ML_0 for SC simulations, but substantially decreases with increasing ML_0 for MC simulations, showing that this qualitative variation trend for MC-fuel drops cannot be captured by the SC approximation.

4.4.3. *Vapor-fuel composition and gas temperature*

In SC simulations the fuel-vapor composition is inherently invariant. The impact of MC-fuel drop evaporation on the gas phase is illustrated in Fig. 16 showing the timewise evolution of (x_1, x_3)-plane averages for θ_v and σ_v for MC2 (16a and 16b) and MC5 (16c and 16d). Due to the early evaporation of the more volatile components, the mean molar weight increases rapidly in the lower, drop-laden stream. At later times, the drops in the lower stream continue evaporating and releasing species of increasing molar weight while the drops entrained into the layer begin releasing intermediary molar weight species, having already released their light molar weight components. As the drops are transported into the upper layer region, the site of the highest molar weight fractions in the gas phase changes accordingly, and the region occupied by the evaporated species widens. This is consistent with the location of the highest drop-number density being in the upper stream (see Fig.7) and with the cross-stream growth of the fuel-vapor layer (not shown). Finally, the mixing induces the penetration of the intermediary molar-weight species into the lower part of the layer. With increasing ML_0, this penetration occurs earlier, however, the peak in $< \theta_v >$ decreases, indicating a reduced species-stratification of the layer while evaporation in the lower stream ceases, with apparent saturation. The indication of saturation is consistent with the information presented in Fig. 12 showing an asymptotic decrease in the drop size. It is now clear that in the upper part of the layer the drop size may evolve to be nearly constant, but this is the result of

evaporation/condensation process, whereas in the lower stream the nearly constant drop size is an indication of saturation. This interpretation is supported by the plots in Figs. 16b and 16d illustrating $< \sigma_v >$. Concomitant to the increase in $< \theta_v >$, $< \sigma_v >$ exhibits a similar augmentation. At earlier times, $< \sigma_v >$ augmentation occurs in the region adjacent to the boundary between the two streams because this is where the drops encounter the highest temperature (since the gas temperature in the lower stream initially decreases due to heat transfer to the drops) and begin evaporating. The central peak in Figs. 16b and 16d at $t^* = 25$ is equivalent to the corresponding peak in Figs. 16a. and 16c. The variance continues to display the largest augmentation in the region of strongest drop evaporation, as increasingly heavier components are released from the drops. At transition, the largest variance is in the upper part of the layer, indicating a more inhomogeneous molar weight region; the inhomogeneity decreases with increasing ML_0, emulating the $< \theta_v >$ results. As one progresses towards the middle layer region, an abrupt reduction followed by a local peak is encountered, reminiscent of the non-uniformity in composition (e.g. Figs. 7e and 7f) around localities of high ρ_n (e.g. Figs. 7c and 7d). In the middle part of the layer, $< \sigma_v >$ displays a plateau for $ML_0 = 0.2$, indicating a more uniform composition, while for $ML_0 = 0.5$ there is a gradual reduction from the upper to the lower part of the layer; this information reminds that of Figs. 7e and 7f which depicted the between-the-braid plane. At the lower extremity of the layer, another local peak is evident, but at a smaller $< \sigma_v >$ than at the upper extremity of the layer, corresponding to the cross-stream locations of large ρ_n and larger $< \theta_v >$-cross-stream variation, an example of which is clearly seen in Fig.7. The smallest variance is in the lower stream, indicating the most homogeneous region; while the variance exhibits only a minimal timewise variation for $ML_0 = 0.2$, it displays no variation (on this $< \sigma_v >$ scale) for $ML_0 = 0.5$, which completes the information indicative of saturation.

The volume-averaged gas temperature is depicted in Fig. 17. Initially, $<< T_g >>$ decreases for both SC and MC cases. However, as the MC-fuel drop evaporation rate decreases, $<< T_g >>$ remains larger since the heat transfer is reduced. The $ML_0 = 0.5$ simulations exhibit a plateau corresponding to the shallow part of the $\{\{T_d\}\}$ curves in Fig. 15 representing the duration between roll-up and conclusion of the first pairing. The further reduction in $<< T_g >>$ mirrors the second augmentation in $\{\{T_d\}\}$ occurring after the first pairing.

5. Conclusions

A study of a multicomponent drop-laden three-dimensional mixing layer has been conducted by adopting the continuous thermodynamics approach to mathematically describe the liquid composition in a probabilistic manner. Following previous continuous thermodynamics representations, the distribution of the chemical species in the fuel is described by a function of the molar weight. Initially, the layer is laden with drops in the lower stream and the drop temperature is lower than that of the carrier gas. Drop evaporation leads to a change in the gas phase composition, which is also described in a probabilistic manner. A model for the MC-fuel drop-laden mixing layer has been developed by assuming the initial mathematical form of the distribution function and postulating that the same form is retained during the drop lifetime, but with evolving mean and variance as the drops evaporate. Therefore, the physical complexity of the MC situation was mathematically translated to only two additional equations being solved (one for the mean, and one for the second moment) for each liquid and gas.

A test of the isolated drop model using this probabilistic approach was conducted and has shown that when the initial liquid-species distribution is narrow and has the same mean molar weight as the single-component fuel, the diameter predicted by the

multicomponent model compares favorably with that of the single-component model. Further, isolated multicomponent-fuel drop calculations were conducted with diesel and gasoline fuels to elucidate their behavior when compared to that of n-decane.

The results from four mixing layer simulations were considered, where two simulations performed with diesel-fuel drops were compared with two other simulations conducted with n-decane drops by Okong'o & Bellan (2002a). Except for the liquid properties (density, composition and thermophysical properties), all initial conditions based on the Mach, Reynolds, Prandtl and Schmidt numbers, on the Stokes number probability distribution function, on the drop and gas temperature and on the gas composition were the same in all calculations. However, due to the different fuel density, the specification of the same initial Stokes number probability distribution function lead to smaller initial drop diameters and larger initial number of drops in the multicomponent case compared to the single-component equivalent.

The mixing layer simulations consisted of the perturbation-induced double pairing of four initial vortices to yield an ultimate vortex within which small scales proliferated. The global properties of the layers (momentum thickness, enstrophy, positive spanwise vorticity and vorticity budgets) displayed modest sensitivity to the fuel composition and the layers attained transition at similar times. Visualizations of dynamic and thermodynamic variables showed, however, that the details of the multicomponent-fuel layers differ from their single-component counterpart. Multicomponent-fuel drops evaporated slower due to the higher saturation pressure of the heavier species, leading to their interaction time with the flow being longer. This longer interaction time permitted the development of a more complex small-scale vorticity structure in the flow, and the creation of regions of higher drop number density which also displayed more structure, particularly in high strain regions, than in the single-component fuel simulation. The last feature

was the combined result of single-component fuel drops becoming evaporated, and thus being removed from the computation, and of the initially smaller number of drops, as explained above. In the single-component case, the molar weight of the evaporated fuel was inherently constant and its spatial distribution followed that of the evaporated fuel mass fraction. For the multicomponent drop case, evaporation leads to the mean molar weight in the liquid increasing and the variance initially decreasing. However, as drops were transported into regions of different gas compositions, condensation occurred, leading to an eventual increase of the liquid variance. This realistic condensation of some species coexisting with the evaporation of other species was captured with only two additional conservation equations compared to the single-component fuel situation. The slower evaporation and the evaporation/condensation process were considered responsible for the reduced drop-size polydispersity in multicomponent simulations compared to their single-component counterpart. The species released from the drop contributed to increasing both the mean molar weight and the variance of the gas composition. Visualization of the mean molar weight spatial distribution in streamwise planes revealed that the lighter components accumulated in the lower stream as they were released early during evaporation, before the drops were entrained in the layer. Intermediary molar weight species resided in the interior of the layer because they were released after the drops were entrained and therefore participated in the mixing process resulting from the double vortex pairing. The heavier components, which were released later in the drop lifetime, resided in regions of high drop-number density. Therefore, a segregation of the chemical species occurred based on the time of their release from the drops. It is this segregation, which is important in combustion processes, that cannot be captured by the single-component fuel drop approximation.

Further investigations of multicomponent-fuel drop representation will focus on im-

proving the robustness of the present model. Indeed, tests with gasoline (which is more volatile than diesel fuel) or with diesel-fuel drops in a higher initial-temperature carrier gas, revealed that as evaporation becomes faster the model breaks down. This indicates that the assumed invariant mathematical form of the molar-weight distribution during drop evaporation is not a good assumption. A robust physical representation of the fuel composition should allow the study of a variety of fuels and in environments at higher gas temperatures than for single-component fuels for which Direct Numerical Simulation results are of interest only if the gas temperature is low enough to allow survival of the drops long enough to interact with the flow. In contrast, equivalent multicomponent-fuel drop simulations do not have this limitation and have the potential of elucidating the evolution of transitional features of the flow at different temperatures.

This research was performed at the Jet Propulsion Laboratory (JPL) of the California Institute of Technology, under the partial sponsorship of the Donors of The Petroleum Research Fund, administered by the American Chemical Society. Additional sponsorship was provided by U.S. Department of Energy (DOE), with Mr. Neil Rossmeissl (DOE Headquarters) and Mr. D. Hooker (DOE Golden Center) serving as contract monitors, under an agreement with the National Aeronautics and Space Administration. The authors wish to thank Dr. Kenneth Harstad of JPL for many helpful discussions on thermodynamics and Dr. Nora Okong'o of JPL for help with numerical and computational aspects. Computational resources were provided by the supercomputing facility at JPL.

Appendix A. Consistent boundary conditions

The Characteristic Boundary Conditions (NSCBC) method in the context of the Local One-Dimensional Inviscid (LODI as in Poinsot & Lele (1992) and Baum *et al.* (1994))

was here implemented to derive boundary conditions. This new derivation is necessary because the molar weight becomes a variable in the context of CT. The CT-modified Navier-Stokes system of equations can be written as:

$$\frac{\partial \widetilde{\mathbf{U}}}{\partial t} + \frac{\partial \mathbf{F}^{(k)}}{\partial x_j} + \widetilde{\mathbf{C}}^{(k)} = 0 \tag{A 1}$$

where the set of conservative variables is defined by

$$\widetilde{\mathbf{U}} = (c, cm_{ga}u_j, cE_t, cX_v, cX_v\theta_v, cX_v\psi_v)\,, \tag{A 2}$$

the flux vector of the conservative variables is the following

$$\mathbf{F}^{(k)} = [cu_j, cu_ju_k, (cE_t + p)u_j, cX_vu_j, cX_v\theta_vu_j, cX_v\psi_vu_j] \quad k \in [1,3] \tag{A 3}$$

and $\widetilde{\mathbf{C}}^{(k)}$ includes all terms without any first derivative of $\widetilde{\mathbf{U}}$ along the j direction

$$\begin{aligned}\widetilde{\mathbf{C}}^{(k)} = [&-\frac{\partial}{\partial x_j}c\overline{D}\frac{\partial}{\partial x_j}(X_v) + \frac{1}{m_{ga}}\frac{\partial}{\partial x_j}[c\widetilde{D}\frac{\partial}{\partial x_j}(X_v\theta_v)] - S_{I\text{-mole}}, -\frac{\partial \tau_{kj}}{\partial x_j} - S_{II,k},\\ &-\frac{\partial}{\partial x_j}\left[\lambda\frac{\partial T}{\partial x_j} + u_i\tau_{ij} - \sum_{\beta=[ga,[1,N]]} J_{Dj\beta}h_\beta\right] - S_{III}, -\frac{\partial}{\partial x_j}[c\overline{D}\frac{\partial X_v}{\partial x_j}] - S_{I-\text{mole}}\,,\\ &-\frac{\partial}{\partial x_j}[c\widetilde{D}\frac{\partial}{\partial x_j}(X_v\theta_v)] - S_{I-\text{mass}}, -\frac{\partial}{\partial x_j}c\widehat{D}\frac{\partial}{\partial x_j}(X_v\Psi_v) - S_\Psi].\end{aligned} \tag{A 4}$$

The system of equations is closed by using the perfect gas law for the gas mixture $p = cR_uT$.

In order to identify characteristic waves in the hyperbolic part of our CT-modified system of equations, we derive an equivalent form of the system using the following set of primitive variables $\mathbf{U} = (c, u_j, p, X_v, \theta_v, \psi_v)$. If $\mathbf{P}$ is the matrix transformation from the conservative to the primitive variables

$$\mathbf{P} = \frac{\partial \widetilde{\mathbf{U}}}{\partial \mathbf{U}} \tag{A 5}$$

$$\mathbf{P} = \begin{pmatrix} 1 & 0 & 0 & 0 & 0 & 0 & 0 & 0 \\ mu_1 & mc & 0 & 0 & 0 & cu_1(\theta_v - m_{ga}) & cu_1 X_v & 0 \\ mu_2 & 0 & mc & 0 & 0 & cu_2(\theta_v - m_{ga}) & cu_2 X_v & 0 \\ mu_3 & 0 & 0 & mc & 0 & cu_3(\theta_v - m_{ga}) & cu_3 X_v & 0 \\ \mathbf{P}_{5,1} & cu_1 & cu_2 & cu_3 & \frac{1}{\gamma-1} & \mathbf{P}_{5,6} & \mathbf{P}_{5,7} & 0 \\ X_v & 0 & 0 & 0 & 0 & c & 0 & 0 \\ X_v\theta_v & 0 & 0 & 0 & 0 & c\theta_v & cX_v & 0 \\ X_v\psi_v & 0 & 0 & 0 & 0 & c\psi_v & 0 & cX_v \end{pmatrix} \tag{A 6}$$

where

$$\begin{aligned} \mathbf{P}_{5,1} &= \frac{u_i u_i}{2} + X_v(K\theta_v + K') \\ \mathbf{P}_{5,6} &= p(A_c + B_c\theta_v - \frac{Cp_{ga}}{R_u}) + c(K\theta_v + K') \\ \mathbf{P}_{5,7} &= X_v(pB_c + cK) \end{aligned} \tag{A 7}$$

The wave amplitudes corresponding to each eigenvalue λ_i are

$$\begin{aligned} \mathcal{L}_1 &= (u_2 - c)\left[\frac{\partial p}{\partial y} - mca\frac{\partial u_2}{\partial y}\right] \text{ for } \lambda_1 = u_2 - a \\ \mathcal{L}_2 &= u_2\left[\frac{\partial p}{\partial y} - ma^2\frac{\partial c}{\partial y}\right] \text{ for } \lambda_2 = u_2 \\ \mathcal{L}_3 &= u_2\frac{\partial u_1}{\partial y} \qquad \text{for } \lambda_3 = u_2 \\ \mathcal{L}_4 &= u_2\frac{\partial u_3}{\partial y} \qquad \text{for } \lambda_4 = u_2 \\ \mathcal{L}_5 &= u_2\frac{\partial X_v}{\partial y} \qquad \text{for } \lambda_5 = u_2 \\ \mathcal{L}_6 &= u_2\frac{\partial \theta_v}{\partial y} \qquad \text{for } \lambda_6 = u_2 \\ \mathcal{L}_7 &= u_2\frac{\partial \psi_v}{\partial y} \qquad \text{for } \lambda_7 = u_2 \\ \mathcal{L}_8 &= (u_2 + c)\left[\frac{\partial p}{\partial y} + mca\frac{\partial u_2}{\partial y}\right] \text{ for } \lambda_8 = u_2 + a \end{aligned} \tag{A 8}$$

The cross stream boundaries are adiabatic slip walls, and therefore $\lambda\frac{\partial T}{\partial y} + u_2\tau_{2j} -$

$\sum_{\beta=[ga,[1,N]]} J_{D2\beta} h_\beta = 0$, reflecting the null heat flux condition through the wall. One inviscid condition, $u_2 = 0$, must be satisfied at the slip wall, and the viscous relations are represented by null tangential stresses, $\tau_{12} = \tau_{23} = 0$. Since the normal velocity is null, the amplitudes $\mathcal{L}_2$ through $\mathcal{L}_7$ are zero and $\mathcal{L}_1 = \mathcal{L}_8$. The amplitude of the reflected wave $\mathcal{L}_1$ is thus set to $\mathcal{L}_8$, with $\mathcal{L}_8$ computed from the variables inside the domain.

REFERENCES

ABRAMZON, B. & SIRIGNANO, W. A. 1989 Droplet vaporization model for spray combustion calculations, *Int. J. Heat Mass Transfer*, **32**, 1605-1618.

ANDRÉ J. C. & LESIEUR, M. 1977 Influence of Helicity on the Evolution of Isotropic Turbulence at High Reynolds Number. *J. Fluid Mech.,* 81, 187-207.

BATCHELOR, G. K. 1967 *An Introduction to Fluid Thermodynamics*, Cambridge University Press.

BAUM, M., POINSOT, T. & THÉVENIN, D. 1994 Accurate boundary conditions for multicomponent reactive flows, *J. Comp. Phys.* **116**, 247-261.

BOIVIN, M., SIMONIN, S. & SQUIRES, K. D. 1998 Direct numerical simulation of turbulence modulation by particles in isotropic turbulence, *J. Fluid Mech.*, **375**, 235-263.

CHEN, X. Q. & PEREIRA, J. C. F. 1996 Computation of turbulent evaporating sprays with well-specified measurements: a sensitivity study on droplet properties, *Int. J. Heat Mass Transfer*, **39**, 441-454.

CHOU, G. F. & PRAUSNITZ, J. M. 1986 Adiabatic flash calculations for continuous or semicontinuous mixtures using an equation of state, *Fluid Phase Equilibria*, **30**, 75–82.

COTTERMAN, R. L., BENDER, R. & PRAUSNITZ, J. M. 1985 Phase equilibria for mixtures containing very many components. Development and application of continuous thermodynamics for chemical process design, *Ind. Eng. Chem. Process Des. Dev.*, **24**, 194–203.

CROWE, C. T., CHUNG, J. N. & TROUTT, T. R. 1988 Particle mixing in free shear flows, *Prog. Energy Combust. Sci.*, **14**, 171-194.

GAL-OR, B., CULLINAN, JR., H. T. & GALLI, R. 1975 New thermodynamic-transport theory for systems with continuous component density distributions, *Chem. Eng. Sci.*, **30**, 1085-1092.

HALLETT, W. L. H. 2000 A simple model for the vaporization of droplets with large numbers of components, *Combustion and Flame*, **121**, 334–344.

HARSTAD, K. & BELLAN, J. 1991 A Model of the evaporation of binary-fuel clusters of drops, *Atomization and Sprays*, **1**, 367-388.

LAW, C. K. & LAW, H. K. 1982 A d^2-law for multicomponent droplets vaporization and combustion, *AIAA J.* **20**, 522-527.

LIPPERT, A. M. & REITZ, R. D. 1997 Modeling of multicomponent fuels using continuous distributions with application to droplet evaporation and sprays, SAE paper 97FL-468.

MASHAYEK, F. 1998 Direct numerical simulations of evaporating droplet dispersion in forced low Mach number turbulence, *Int. J. Heat Mass Transfer*, **41**, 2601-2617.

MASHAYEK, F. 1998 Droplet-turbulence interactions in low-Mach-number homogeneous shear two-phase flows, *J. Fluid Mech.*, **367**, 163-203.

MASHAYEK, F. & JABERI, F. A. 1999 Particle dispersion in forced isotropic low-Mach-number turbulence, *Int. J. Heat Mass Transfer*, **42**, 2823-2836.

MILLER, R. S. & BELLAN, J. 1999 Direct numerical simulation of a confined three-dimensional gas mixing layer with one evaporating hydrocarbon-droplet laden stream, *J Fluid Mech.*, **384**, 293–338.

MILLER, R. S. & BELLAN, J. 2000 Direct numerical simulation and subgrid analysis of a transitional droplet laden mixing layer. *Phys. Fluids* **12**, 650–671.

MILLER, R. S., HARSTAD, K. & BELLAN, J. 1998 Evaluation of equilibrium and non-equilibrium evaporation models for many-droplet gas-liquid flow simulations, *Int. J. Multiphase Flow*, **24**, 1025–1055.

MOFFATT, H. K. 1969 The Degree of knottedness of tangle vortex lines. *J. Fluid Mech.*, **35**, 117-129

MOFFATT, H. K. 1985 Magnetostatic equilibria and analogous Euler flows of arbitrarily complex topology. *J. Fluid Mech.*,**159**, 359-378.

MOFFATT, H. K. 1992 Helicity in laminar and turbulent flows *Annu. Rev. Fluid Mech.*, **24**, 281-312.

MOSER, R. D. & ROGERS, M. M. 1991 Mixing transition and the cascade to small scales in a plane mixing layer, *Phys. Fluids A*, **3**, 1128–1134

ROGERS, M. M. & MOSER, R. D. 1991 The three dimensional evolution of a plane mixing layer: the Kelvin-Helmholtz roll-up. *J. Fluid Mech.* **243**, 183–226.

MOSER, R. D. & ROGERS, M. M. 1993 The three dimensional evolution of a plane mixing layer: pairing and transition to turbulence. *J. Fluid Mech.* **247**, 275–320.

OKONG'O, N. & BELLAN, J. 2000 A priori subgrid analysis of temporal mixing layers with evaporating droplets, *Phys. Fluids*, **12**, 1573–1591.

OKONG'O, N. & BELLAN, J. 2002a Consistent large eddy simulation (LES) of a temporal mixing layer laden with evaporating drops. Part I: Direct numerical simulation and analysis of LES equations, to be submitted for publication

OKONG'O, N. & BELLAN, J. 2002b Consistent large eddy simulation (LES) of a temporal mixing layer laden with evaporating drops. Part II: Irreversible entropy production and *a priori* analysis, to be submitted for publication

PELZ, R. B., YAKHOT, V., ORSZAG, S. A., SHTILMAN, L. & LEVICH, E. 1985 Velocity-vorticity patterns in turbulent flow. *Phys. Rev. Lett.*, **54**, 2505-.2508.

PELZ, R. B., SHTILMAN, L. & TSINOBER, A. 1986 The helical nature of unforced turbulent flows. *Phys. Fluids.*, **29**, 3506-3508.

POINSOT, T. J. & LELE, S. K. 1992 Boundary conditions for direct simulations of compressible viscous flows, *J. Comp. Phys.*, **101**, 104–129

RÉVEILLON, J. & VERVISCH, L. 2000 Spray vaporization in nonpremixed turbulent combustion modeling: a single drop model, *Comb. Flame*, **121**, 75-90.

ROGERS, M. M. & MOIN, P. 1987 Helicity fluctuations in incompressible turbulent flows. *Phys. Fluids.*, **30**, 2662-2671.

SQUIRES, K. D. & EATON, J. K. 1991 Preferential concentration of particles by turbulence, *Phys. Fluids A*, **3**, 1169-1178.

SHTILMAN, L., LEVICH, E., ORSZAG, S. A., PELZ, R. B. & TSINOBER, A. 1985 On the role of helicity in complex fluid Flows. *Phys. Lett. A,* **113**, 32-37.

SHTILMAN, L., PELZ, R. B. & TSINOBER, A. 1988 Numerical investigation of helicity in turbulent flows. *Comp. Fluids,* **16**, 341-347.

TAMIM, J. & HALLETT, W. L. H. 1995 A continuous thermodynamics model for multicomponent droplet vaporization, *Chem. Eng. Sci.*, **50**, 2933–2942.

WALLACE, J. W., BALINT, J.-L. & ONG, L. 1992 An Experimental Study of Helicity in Turbulent Flows. *Phys. Fluids. A,* **4**, 2013-2026.

WHITSON, C. H. 1983 Characterizing hydrocarbon plus fractions, *Soc. Pet. Eng. J.*, **23**, 683-694.

WILLIAMS, F. A. 1965 *Combustion Theory*, Addison-Wesley.

Fuel	ρ_l	$\theta_{l,0}$	$\sigma_{l,0}$	$\gamma_{l,0}$
n-decane	642	142	-	-
gasoline	742	101	31.5	60.5
diesel	828	185	43.0	60.5

TABLE 1. Parameters characterizing the density and distribution function for different fuels. The density is in kg/m^3 and all parameters related to the distribution function are in $kg/kmole$.

Run	fuel	ML_0	$N_{d,0}$	$< d_0 >$, m	t^*	
					peak in $<< \omega_3^+ >> \delta_{\omega,0}/\Delta U_0$	transition
SC2	$n-$decane	0.2	2.28×10^6	8.6×10^{-5}	86	100
SC5	$n-$decane	0.5	5.70×10^6	8.6×10^{-5}	97	105
MC2	diesel	0.2	2.70×10^6	7.6×10^{-5}	98	105
MC5	diesel	0.5	6.50×10^6	7.6×10^{-5}	103	110

TABLE 2. Simulation parameters. For both simulations $M_{c,0} = 0.35$, $Re_0 = 500$, $T_{d,0} = 345K$, and $T_{g,0} = 375K$, $\gamma_{l,0} = 76$. The initial drop size distribution is polydisperse and Gaussian with $< St_0 >= 3$ and $St_{0,rms} = 0.5$. The resolution was $N_1 \times N_2 \times N_3$ =256×288×160 in all simulations. SC2 and SC5 represent databases obtained in Okong'o Bellan (2002a).

p]

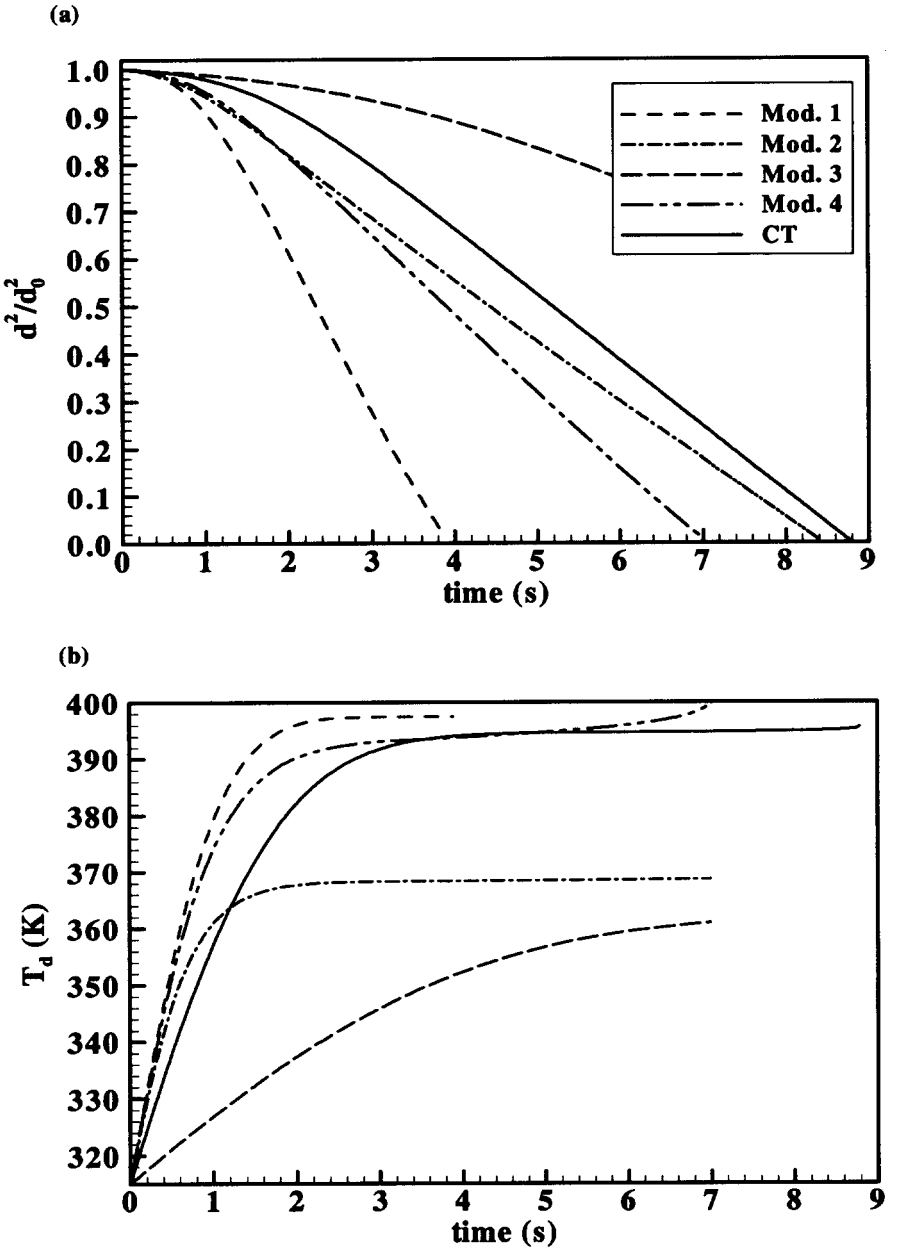

FIGURE 1. Drop evaporation-model comparison. Initial conditions are $T_{ge} = 1000K$, $T_{d,0} = 300K$, $d_0 = 2 \times 10^{-3}m$, and $\mathrm{Re}_{d,0} = 17$, (a) normalized residual drop area, (b) drop temperature.

p]

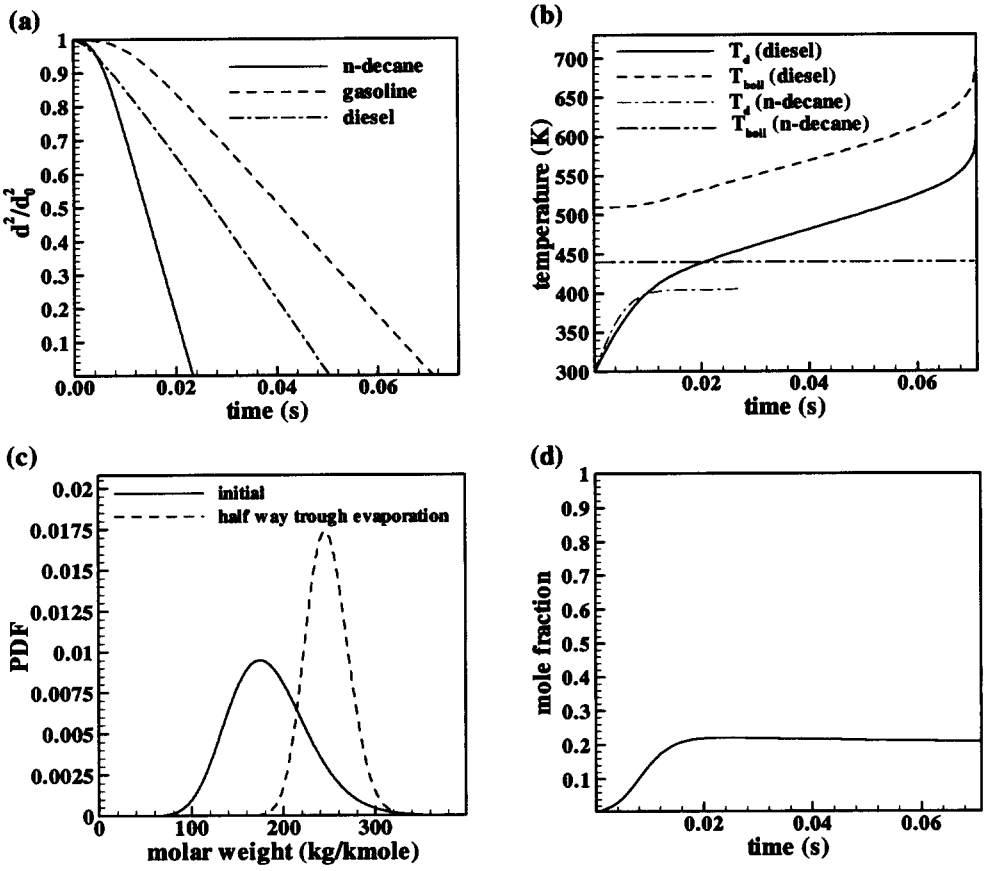

FIGURE 2. Quiescent drop evaporation. Initial conditions: $T_{d,0} = 300K$, $T_{ge} = 1000K$, and $d_0 = 100\mu m$. (a) normalized surface area, (b) drop and liquid boiling temperature evolution, (c) diesel-fuel drop composition evolution and (d) surface mole fraction during diesel-fuel drop evaporation .

p]

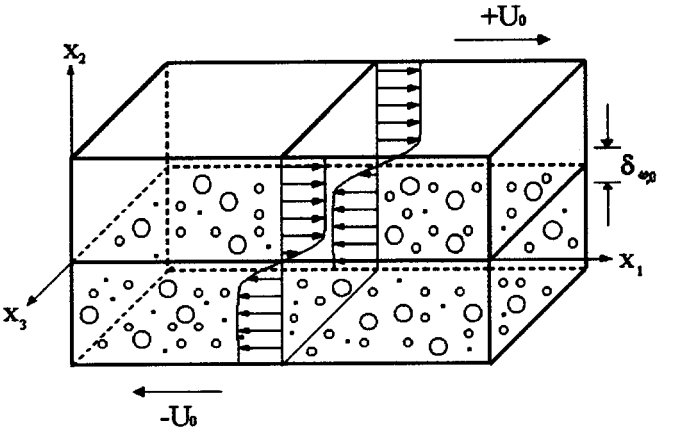

FIGURE 3. Mixing layer configuration.

p]

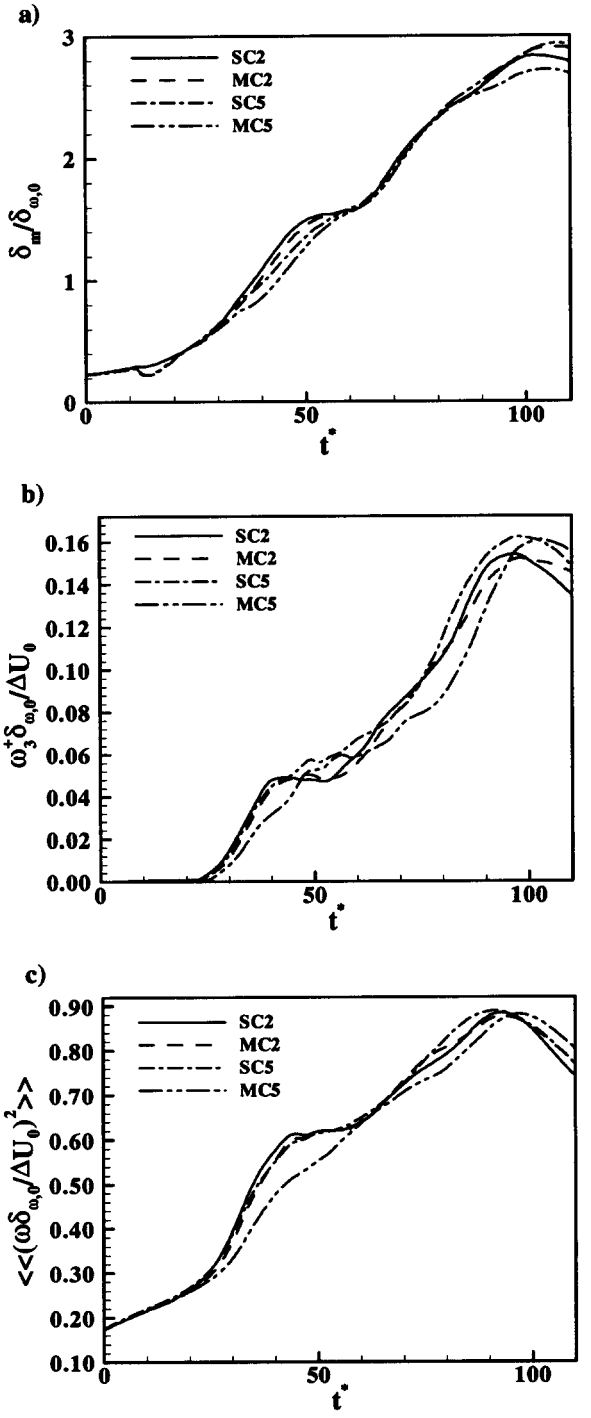

FIGURE 4. Timewise evolution of the non-dimensional momentum thickness, positive spanwise vorticity and enstrophy for the simulations listed in Table 2.

p]

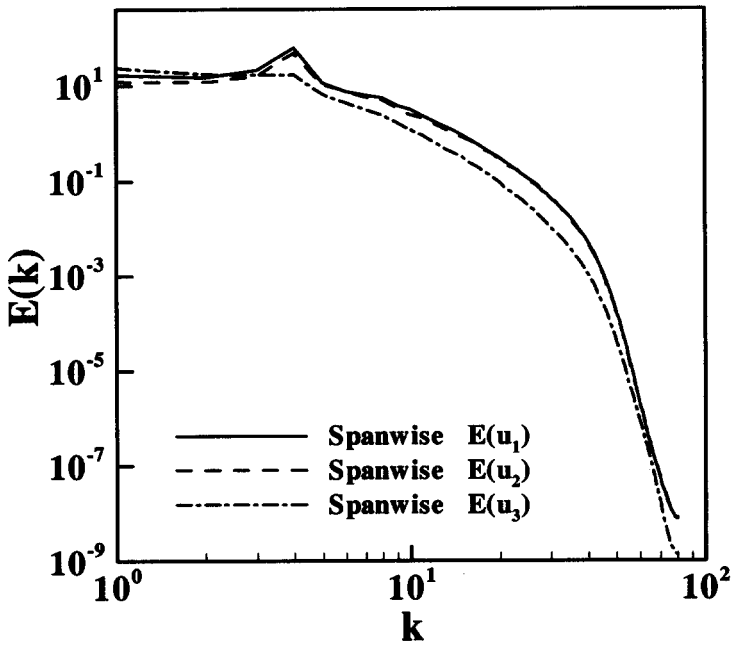

FIGURE 5. Spanwise energy spectra for each component of the velocity fluctuations for MC5 at $t^* = 110$.

p]

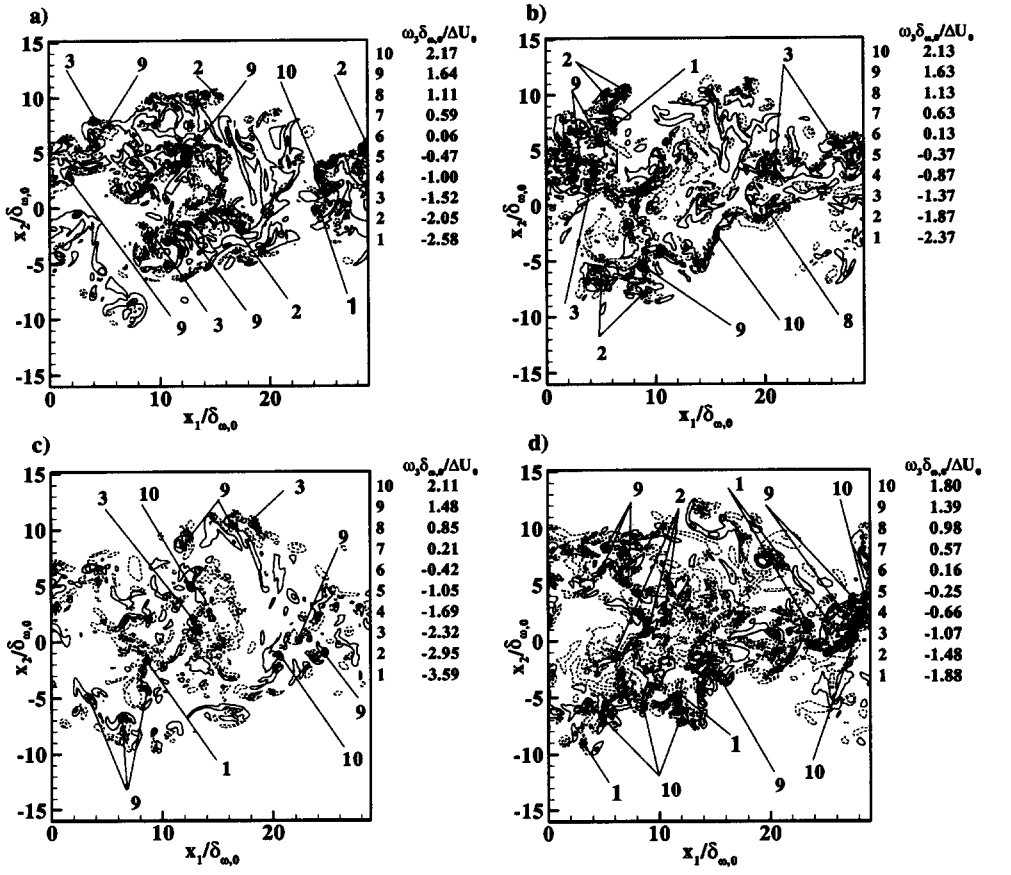

FIGURE 6. Non-dimensional spanwise vorticity in the between-the-braid plane ($x_3 = 0.06$ m) at the transitional time for a) SC2, b) SC5, c) MC2 and d) MC5.

p]

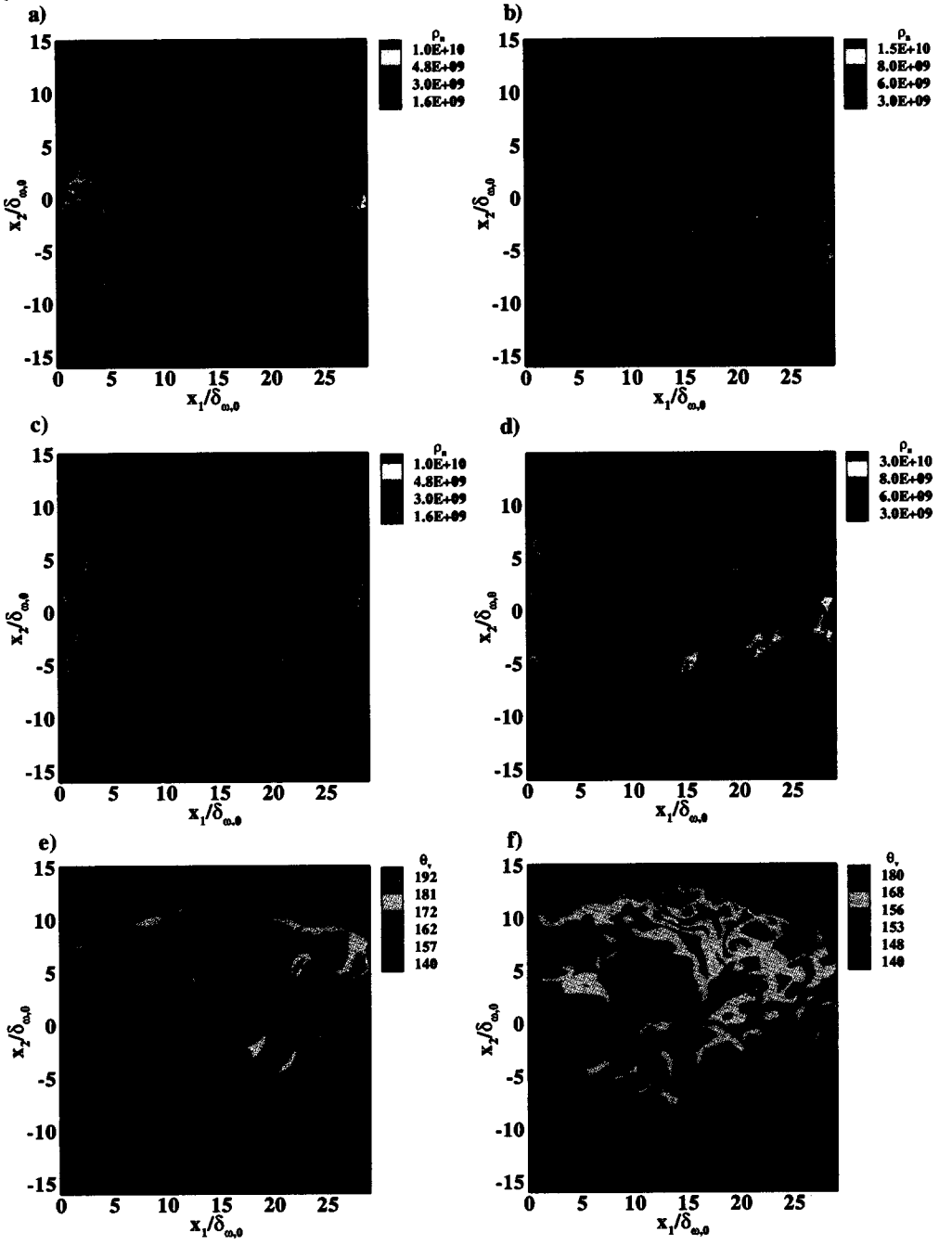

FIGURE 7. Drop number density (a, b, c and d) in m^{-3}, and mean molar weight of the evaporated species (e and f) in kg/kmole plotted in the between-the-braid plane (x_3 = 0.06 m) at the transitional time for a) SC2, b) SC5, c) MC2, d) MC5, e) MC2 and f) MC5.

p]

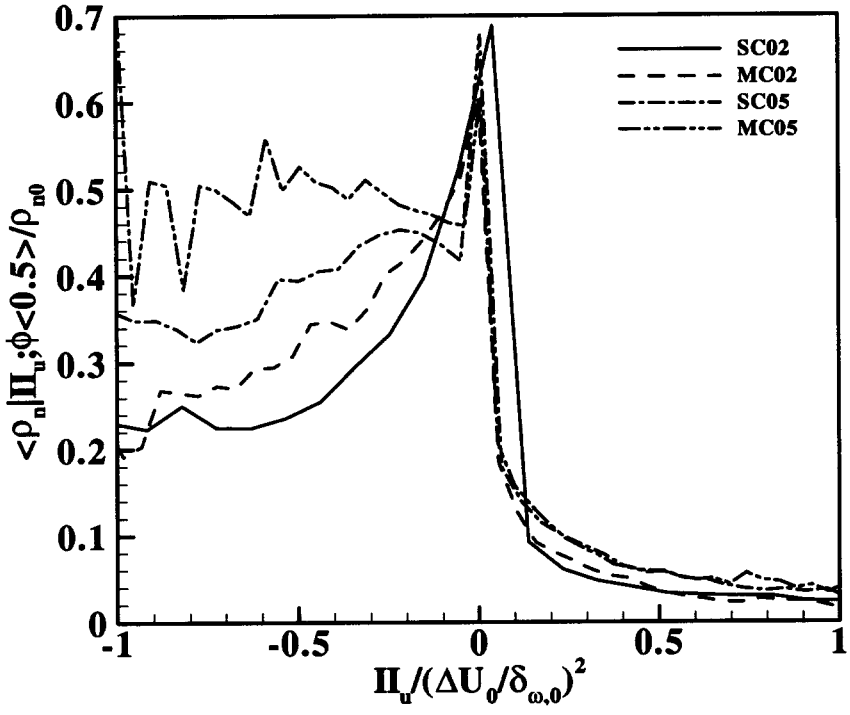

FIGURE 8. Drop number density at the transitional times conditioned on the second invariant and on a passive scalar being smaller than 0.5.

p]

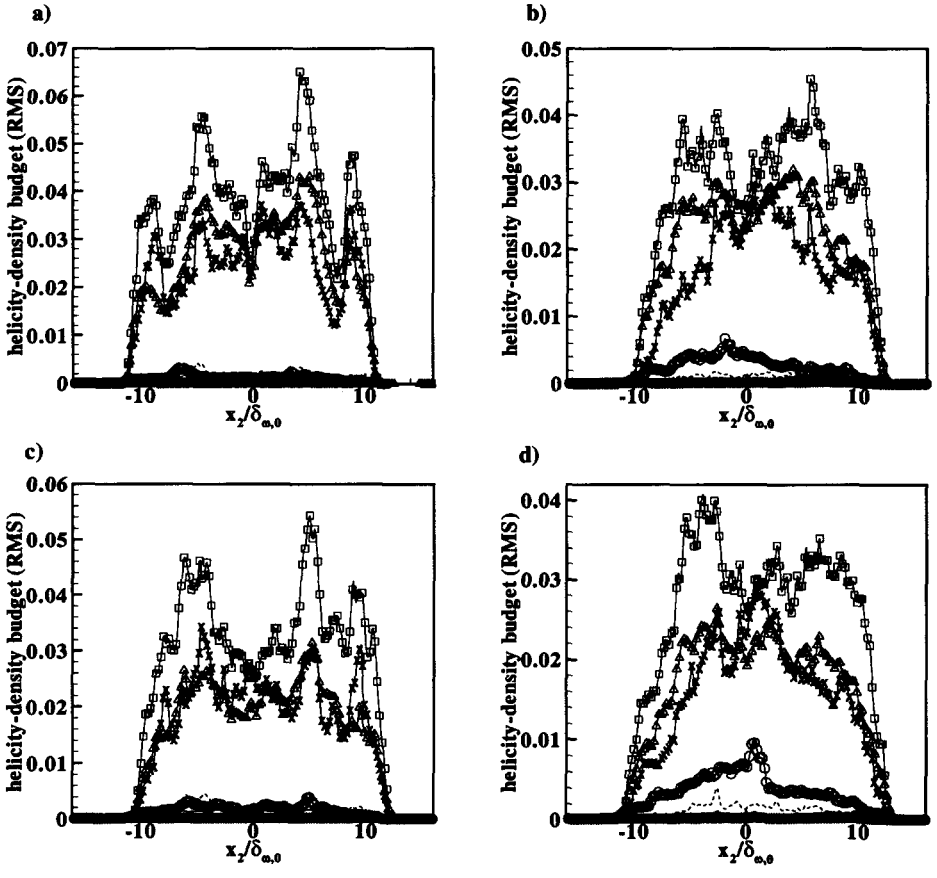

FIGURE 9. Helicity-density RMS budget at transition for a) SC2, b) SC5, c) MC2 and d) MC5 simulations. The legend is: — — stretching/tilting; — — — dilatation; — · — baroclinic; — × — vorticity/pressure-gradient scalar product term; — Δ — viscous effects; — ◯ — momentum-source terms; —— evaporation-source terms.

p]

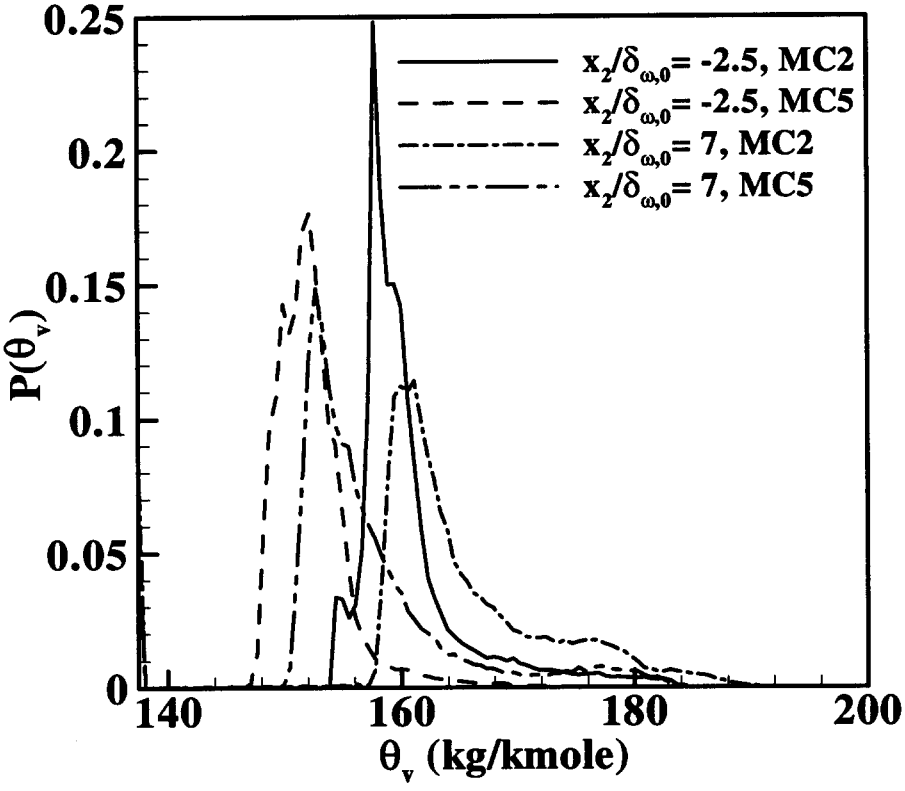

FIGURE 10. PDF of θ_v at different cross-stream locations, $x_2/\delta_{\omega,0}$ = -2.5 and 7 for both MC2 and MC5 layers.

p]

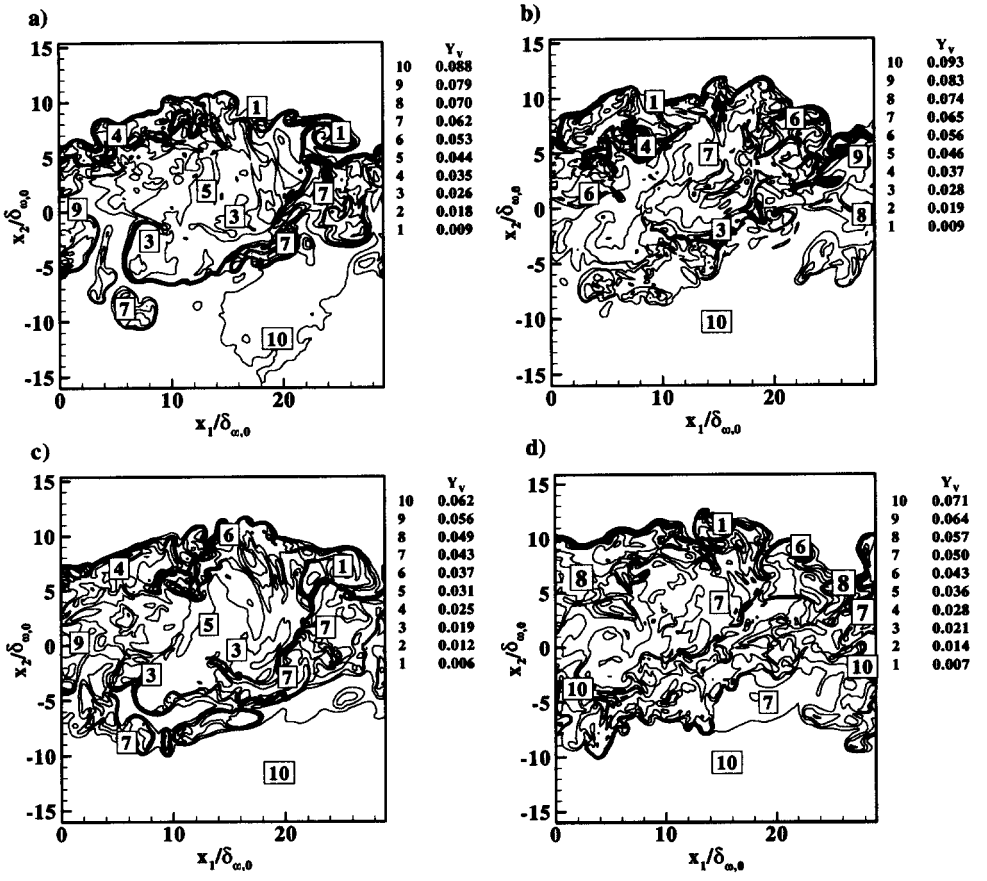

FIGURE 11. Mass fraction of the evaporated species in the between-the-braid plane ($x_3 = 0.06$ m) at the transitional time for a) SC2, b) SC5, c) MC2 and d) MC5.

p]

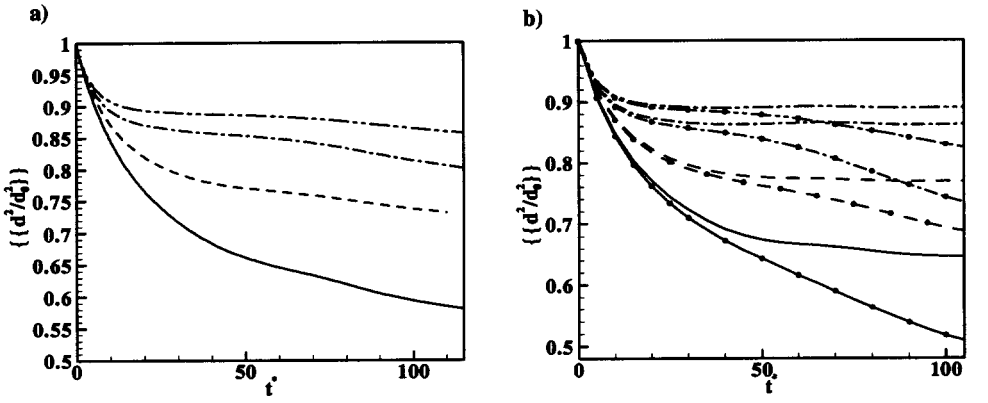

FIGURE 12. Timewise evolution of the Lagrangian average residual droplet area for the SC and MC simulations.—— SC2; – – – MC2; – · – SC5; – · · – MC5 and a) for the entire domain, b) separately for the lower stream (lines) defined as $x_2/\delta_{\omega,0} < -7$ and the mixing layer (lines and symbols).

p]

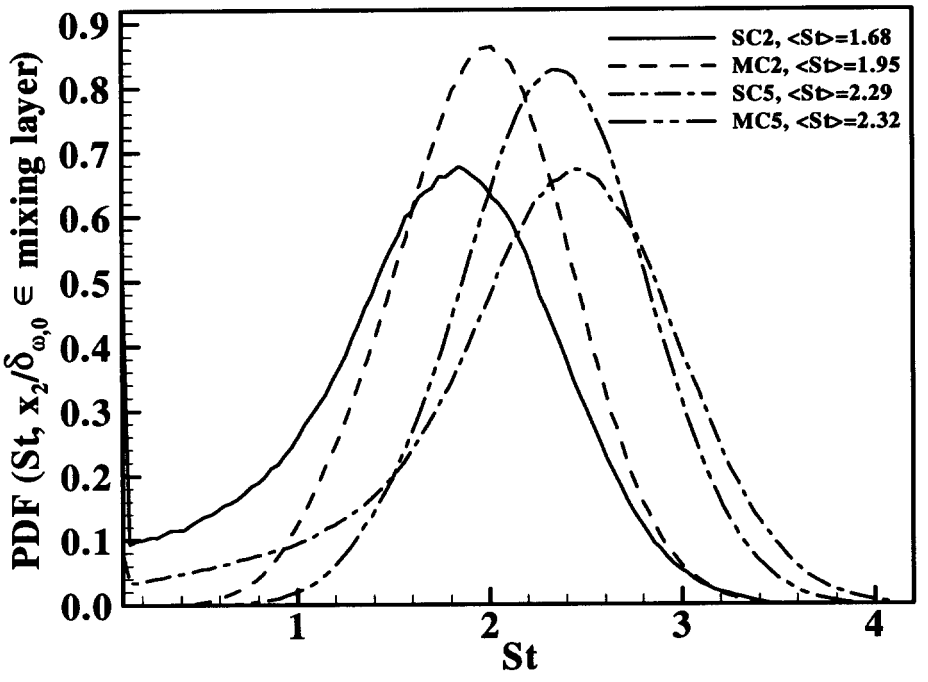

FIGURE 13. Probabilty density functions of drop Stokes number inside the mixing layer (defined as $x_2/\delta_{\omega,0} \geqslant -7$), each at the transitional time.

p]

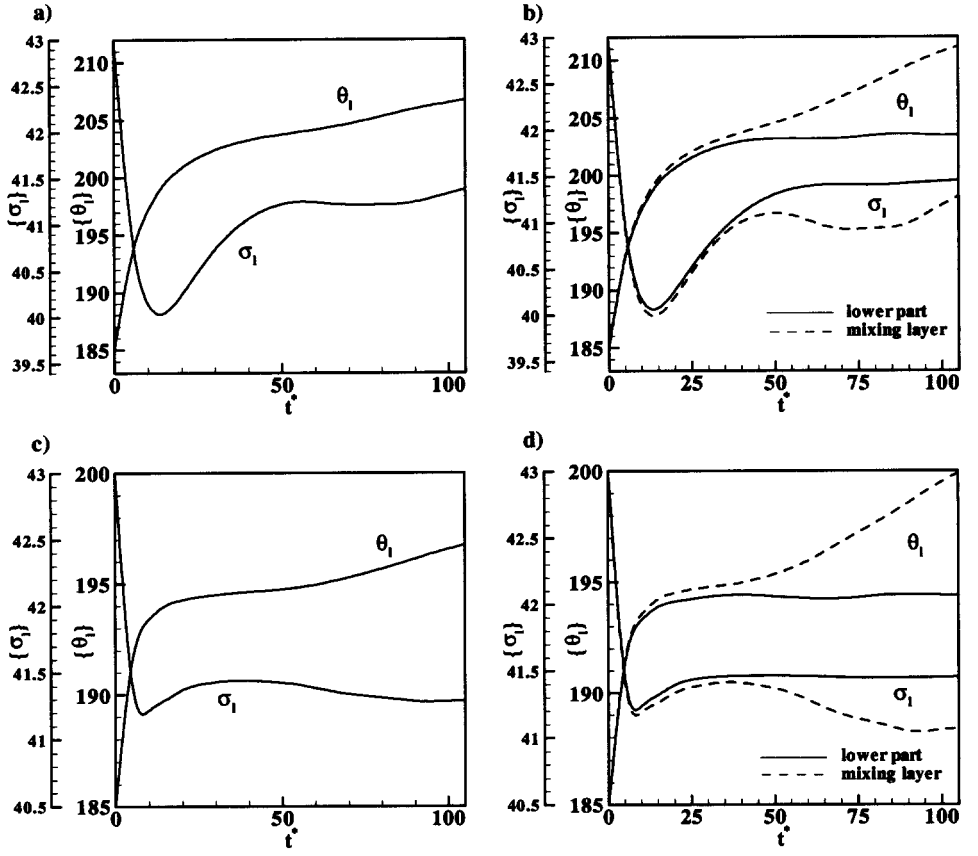

FIGURE 14. Timewise evolution of the liquid composition in MC simulations: mean molar weight and variance in kg/kmole. a) and c) Lagrangian ensemble averages over the entire domain for MC2 and MC5, respectively. b) and d) Separate Lagrangian ensemble averages, for MC2 and MC5, respectively, over the lower stream, defined as $x_2/\delta_{\omega,0} < -7$, and the mixing layer, defined as the remaining part of the domain.

p]

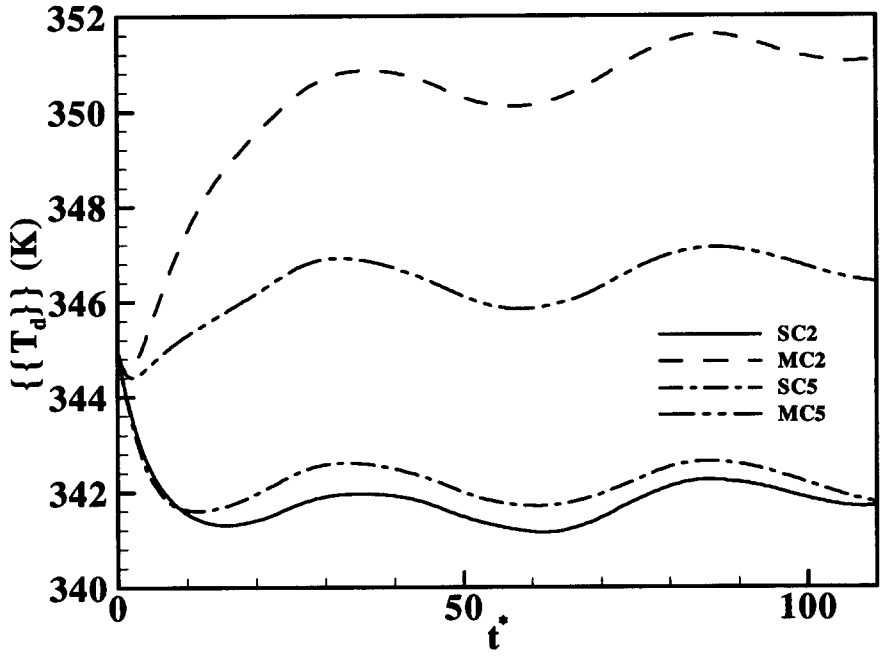

FIGURE 15. Timewise evolution of the ensemble averaged drop temperature for SC and MC simulations.

p]

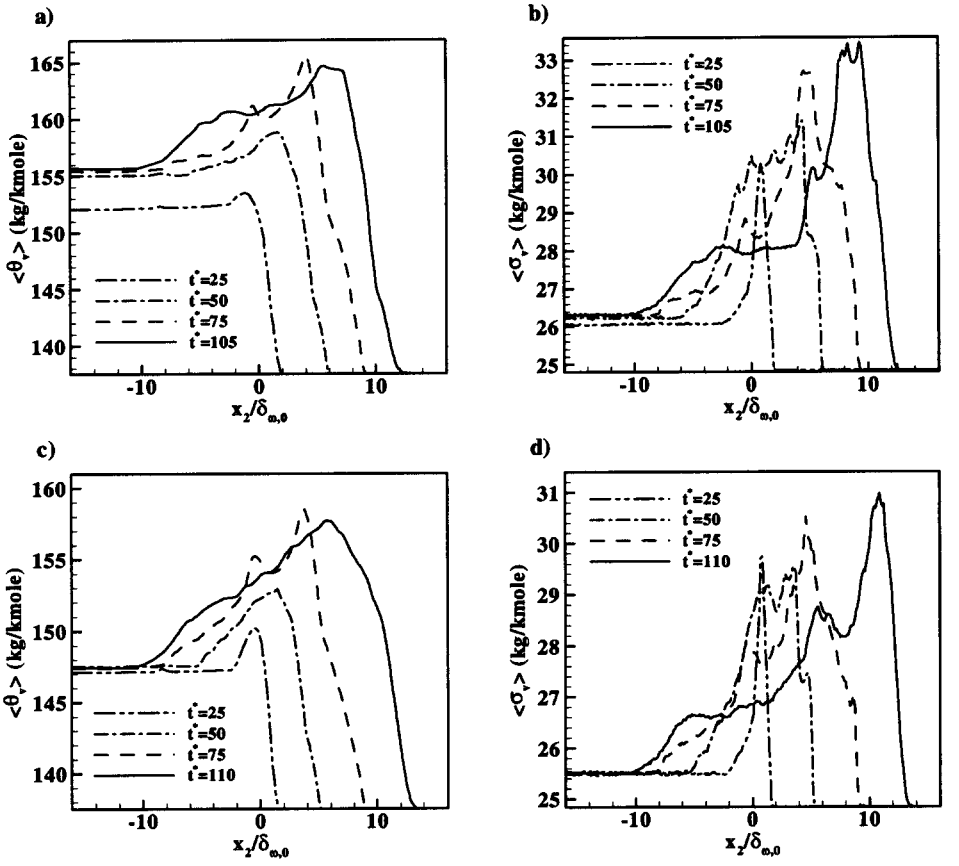

FIGURE 16. Evolution of (x_1, x_3)-plane averages for a) and c) the vapor mean molar weight; b) and d) the vapor distribution-function variance. a) and b) for MC2; c) and d) for MC5. The times correspond to rollup, end of the first pairing, end of the second pairing and transition.

p]

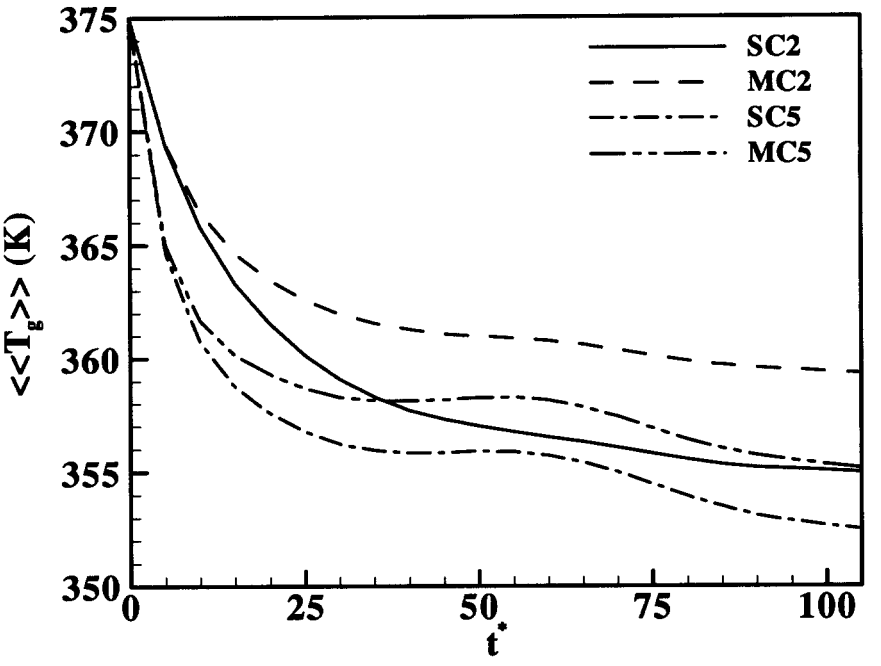

FIGURE 17. Timewise evolution of the volume averaged gas temperature for the SC and MC simulations.